

## X-ray Constraint on Location of AGN Torus in Circinus Galaxy

RYOSUKE UEMATSU,<sup>1</sup> YOSHIHIRO UEDA,<sup>1</sup> ATSUSHI TANIMOTO,<sup>2</sup> TAIKI KAWAMURO,<sup>3,4</sup> KENTA SETOGUCHI,<sup>1</sup> SHOJI OGAWA,<sup>1</sup>  
SATOSHI YAMADA,<sup>1</sup> AND HIROKAZU ODAKA<sup>2,5</sup>

<sup>1</sup>*Department of Astronomy, Kyoto University, Kyoto 606-8502, Japan*

<sup>2</sup>*Department of Physics, The University of Tokyo, Tokyo 113-0033, Japan*

<sup>3</sup>*National Astronomical Observatory of Japan, Tokyo 181-8588, Japan*

<sup>4</sup>*Núcleo de Astronomía de la Facultad de Ingeniería, Universidad Diego Portales, Av. Ejército Libertador 441, Santiago, Chile*

<sup>5</sup>*Kavil IPMU, The University of Tokyo, Chiba 277-8583, Japan*

### ABSTRACT

The location of the obscuring “torus” in an active galactic nucleus (AGN) is still an unresolved issue. The line widths of X-ray fluorescence lines originated from the torus, particularly Fe K $\alpha$ , carry key information on the radii of line emitting regions. Utilizing XCLUMPY (Tanimoto et al. 2019), an X-ray clumpy torus model, we develop a realistic model of emission line profiles from an AGN torus where we take into account line broadening due to the Keplerian motion around the black hole. Then, we apply the updated model to the best available broadband spectra (3–100 keV) of the Circinus galaxy observed with Suzaku, XMM-Newton, Nuclear Spectroscopic Telescope Array (NuSTAR), and Chandra, including 0.62 Ms Chandra/HETG data. We confirm that the torus is Compton-thick (hydrogen column-density along the equatorial plane is  $N_{\text{H}}^{\text{Equ}} = 2.16_{-0.16}^{+0.24} \times 10^{25} \text{ cm}^{-2}$ ) geometrically thin (torus angular width  $\sigma = 10.3_{-0.3}^{+0.7}$  degrees), viewed edge-on (inclination  $i = 78.3_{-0.9}^{+0.4}$  degrees), and has super-solar abundance ( $1.52_{-0.06}^{+0.04}$  times solar). Simultaneously analyzing the Chandra/HETG first, second, and third order spectra with consideration of the spatial extent of the Fe K $\alpha$  line emitting region, we constrain the inner radius of the torus to be  $1.9_{-0.8}^{+3.1} \times 10^5$  times the gravitational radius, or  $1.6_{-0.9}^{+1.5} \times 10^{-2}$  pc for a black hole mass of  $(1.7 \pm 0.3) \times 10^6 M_{\odot}$ . This is about 3 times smaller than that estimated from the dust sublimation radius, suggesting that the inner side of the dusty region of the torus is composed of dust-free gas.

*Keywords:* Active galactic nuclei (16), Astrophysical black holes (98), High energy astrophysics (739), Seyfert galaxies (1447), Supermassive black holes (1663), X-ray active galactic nuclei (2035)

### 1. INTRODUCTION

Formation mechanisms of supermassive black holes (SMBHs) in galactic centers are an important topic in modern astronomy, which are related to the understanding of galaxy-SMBH coevolution (see e.g., Kormendy & Ho 2013 for a review). An active galactic nucleus (AGN) is a key object to tackle this problem because it represents the process of SMBH growth by mass accretion. One of the major remaining questions in AGN phenomena is mass feeding processes onto SMBHs. Past studies have built a consensus that the central engine of an AGN is surrounded by obscuring material called a

“torus”<sup>1</sup> (see e.g., Ramos Almeida & Ricci 2017 for a recent review). This torus is considered to be a link between the inner accretion disk and host-galaxy scale gas playing as a reservoir supplying mass toward the central SMBH. Hence, elucidating the nature of AGN tori is indispensable to understand the physical origin of AGN feeding.

X-ray observations are powerful tool to study AGN tori because X-rays have strong penetrating power and serve as an unbiased tracer of material in various phys-

<sup>1</sup> In this paper, we use the term “torus” as the whole structure of X-ray obscuring material including possible dust-free gas at the innermost region. In this context, our “torus” is not the same as “dust (or dusty) torus” often referred to in optical and infrared astronomy.

ical conditions, including gas and dust. Several groups developed X-ray spectral models that reproduce reflection components (including Compton reflection continuum and fluorescence lines) from a torus with a simplified geometry (e.g., Murphy & Yaqoob 2009, Ikedo et al. 2009, Brightman & Nandra 2011, Baloković et al. 2018). Many studies show that an AGN torus is not smooth but is composed of clumpy media. Accordingly, Tanimoto et al. (2019) have constructed a new X-ray clumpy torus model called XCLUMPY, utilizing the Monte Carlo simulation for astrophysics and cosmology framework (MONACO: Odaka et al. 2011, 2016)(see also Buchner et al. 2019 for a similar X-ray clumpy torus model). XCLUMPY assumes the same distribution of clumps as that in the infrared clumpy torus model CLUMPY constructed by Nenkova et al. (2008a,b). By applying XCLUMPY to broadband X-ray spectra of nearby AGNs, Tanimoto et al. (2020), Yamada et al. (2020), and Ogawa et al. (2021) constrained their basic torus parameters, such as the torus angular width (torus scale height relative to radius) and column density. These works are consistent with the existence of a relation between torus covering factor and Eddington ratio, as reported by Ricci et al. (2017).

A key parameter to understand the whole structure of an AGN is the inner radius (i.e., the distance from the SMBH) of the torus. Optical and infrared reverberation observations of nearby AGNs have determined the innermost radii of “dusty” regions in their tori (e.g., Koshida et al. 2009), which are found to be proportional to the square root of AGN luminosity as theoretically expected (Kawaguchi & Mori 2010). However, it remains unclear whether or not there is a significant amount of dust-free gas that cannot be probed by infrared observations inside the dust sublimation radius. Unfortunately, most of previous X-ray studies were not able to constrain it because the torus models used are “scale-free”, that is, tori of a similar geometrical form with different absolute scales produce exactly the same reflection component including the continuum and lines.

High resolution X-ray spectroscopy has a great potential to constrain the true innermost radius of an AGN torus including dust-free gas. In AGN X-ray spectra, most of the narrow fluorescence lines from cold material are believed to come from the torus, among which Fe  $K\alpha$  at 6.4 keV is the strongest (see e.g, Reynolds et al. 2014). Assuming that the motion of torus matter basically obeys Keplerian rotation around the SMBH, it is possible to estimate the radius by measuring the line width (or ideally, line profile) due to Doppler broadening. Minezaki & Matsushita (2015) and Gandhi et al. (2015) estimated the radii of Fe  $K\alpha$  line emitting re-

gions in nearby AGNs. They referred to the Fe  $K\alpha$  line widths compiled by Shu et al. (2010, 2011) using the Chandra/HETG data. However, it has been pointed out that these measurements might be subject to systematic uncertainties. Firstly, Shu et al. (2010, 2011) approximately fitted the Fe  $K\alpha$  line by a single-Gaussian model. In reality, Fe  $K\alpha$  line consists of two lines ( $K\alpha_1$ ,  $K\alpha_2$ ) often accompanied by Compton shoulders. Secondly, the grating spectra may be affected by spatial extent of the emitting region. Liu (2016a) reported that the Chandra/HETG first order spectra of nearby AGNs systematically showed broader line widths than the higher order ones. This can be explained by the spatial extent, to which the first order spectra are the most sensitive.<sup>2</sup>

In this paper, we update the fluorescence line component of the XCLUMPY model by including line broadening effects due to the Keplerian motion around the SMBH. Then, we apply it to the best available X-ray data observed with Suzaku, XMM-Newton, NuSTAR, and Chandra (including Chandra/HETG data of total 0.62 Ms) of the Circinus galaxy ( $z = 0.0014$ ). To reliably estimate the torus inner radius, we simultaneously analyze the first, second, and third order spectra of the Chandra/HETG by taking into account the source extent of the Fe  $K\alpha$  line emitting region. The structure of this paper is as follows. In Section 2, we describe the update of the XCLUMPY model. Sections 3 and 4 present the observations and the results of the spectral analysis, respectively. Section 5 focuses on a detailed analysis of the Fe  $K\alpha$  line. In Section 6, we compare our result with previous works and discuss the implication. For the Circinus galaxy, we assume a distance of 4.2 Mpc (Freeman et al. 1977) when calculating luminosities and spatial scales. The Solar abundances of Anders & Grevesse (1989) are adopted. An attached error corresponds to the 90% confidence region for a single parameter.

## 2. XCLUMPY MODEL UPDATE

For our study, we update the original XCLUMPY model (Tanimoto et al. 2019) by taking into account (1) Doppler line broadening by the Keplerian motion of each clump and (2) variable metal abundance. We explain the first part below (Section 2.1, 2.2). Hikitani et al. (2018) suggested that the metal abundance of the Circinus galaxy were super-solar ( $\approx 1.7$ ) with Compton-shoulder diagnostics of the Fe  $K\alpha$  line in a fixed torus geometry, whereas Tanimoto et al. (2019) showed that the fraction of the Compton shoulder also depended on torus geometry and column density. To solve the de-

<sup>2</sup> [https://cxc.harvard.edu/newsletters/news\\_24/](https://cxc.harvard.edu/newsletters/news_24/)

generacy, we newly introduce the metal abundance parameter, defined as the ratios to the Solar values, which ranges from 1.0 to 1.8 with a step of 0.2.

### 2.1. Geometry of XCLUMPY Model

Here we briefly review the torus geometry of the XCLUMPY model. XCLUMPY assumes a power-law distribution of spherical clumps with a fixed radius of  $R_{\text{clump}}$  in the radial direction within the inner and outer radii ( $r_{\text{in}}$  and  $r_{\text{out}}$ ), and normal distribution in the elevation direction. The number density of clumps is expressed in Equation 1 (where we use the spherical coordinate system;  $r$  is a radius,  $\theta$  is a polar angle,  $\phi$  is an azimuthal angle):

$$d(r, \theta, \phi) \propto \left(\frac{r}{r_{\text{in}}}\right)^{-0.5} \exp\left(-\frac{(\theta - \pi/2)^2}{\sigma^2}\right) \quad (1)$$

This model has three variable torus parameters: equatorial hydrogen column density ( $N_{\text{H}}^{\text{Equ}}$ ), torus angular width ( $\sigma$ ), and inclination angle ( $i$ ). The number of clumps along the equatorial plane is set to be 10. [Tanimoto et al. \(2019\)](#) assume  $r_{\text{in}} = 0.05$  pc,  $r_{\text{out}} = 1$  pc, and  $R_{\text{clump}} = 0.002$  pc, although only their scale ratios are meaningful because of the geometric similarity (see Section 1).

### 2.2. Doppler Effects

In the original XCLUMPY model, it was assumed that all clumps were completely at rest. In our updated model, we consider the azimuthal velocity of a clump located at  $r$  and  $\theta$ :

$$v_{\phi} = \sqrt{\frac{GM}{r}} \sin \theta = c \sqrt{\frac{r_{\text{g}}}{r}} \sin \theta, \quad (2)$$

where  $G$  is the gravitational constant,  $M$  the black hole mass,  $c$  the light speed, and  $r_{\text{g}} \equiv GM/c^2$  the gravitational radius. It assumes the balance between the centrifugal force and gravity force projected onto the equatorial plane (see Figure 2.2). For simplicity, we ignore any velocity field in the elevation direction, which is not important for the spectra of edge-on sources (like the Circinus galaxy).

To save computation time, we do not repeat Monte Carlo simulations by fully taking into account the motions of clumps in all interactions (e.g., Compton scattering and photoelectric absorption of continuum photons). Instead, as an approximation, we only consider the motion of a clump that emits or scatters a fluorescence-line photon at its last interaction. This enables us to perform a post analysis of the photon event files that were used to make the table models of

XCLUMPY. Although Doppler broadening of absorption edge features in the reflection continuum cannot be reproduced with this approximation, it is sufficient for studies focusing on the profile of emission lines. In the simulation of MONACO, the last interaction point and the last direction of each photon are recorded. Then, we correct the energy and weight of each photon for the Doppler and relativistic beaming effects, respectively, to produce a new table model of the fluorescence lines. Since a Keplerian velocity is determined by the ratio of the radius to the gravitational radius, we introduce the parameter  $\log(r_{\text{in}}/r_{\text{g}})$ , which ranges from 4.0 to 7.0 with a step of 0.5.

In Appendix D, we present examples of the Fe  $K\alpha$  line profiles, together with the spatial distribution of photon emitting positions, for 4 different sets of the torus parameters.

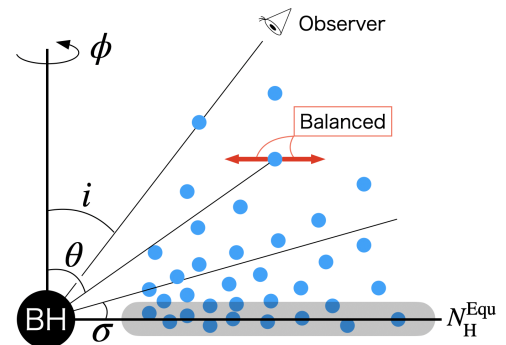


**Figure 1.** Geometry of the XCLUMPY model.  $N_{\text{H}}^{\text{Equ}}$  is the equatorial hydrogen column density,  $\sigma$  the torus angular width, and  $i$  the inclination angle. The red arrows represent the force balance of a clump.

## 3. OBSERVATIONS AND DATA REDUCTION

We have selected the Circinus galaxy ( $z = 0.0014$ ), one of the closest type 2 AGN, as our target. The Circinus galaxy is ideal for our study because it shows the brightest narrow Fe  $K\alpha$  line among all AGNs ([Fukazawa et al. 2011](#)) and because very deep Chandra/HETG data of 681 ks are available ([Arévalo et al. 2014](#)). Since it is a heavily obscured, Compton-thick AGN, one can fairly assume that its Fe  $K\alpha$  line is dominated by the emission from the torus and that the contribution from the accretion disk is ignorable. In this paper, we analyze the X-ray data obtained with Suzaku, XMM-Newton, NuSTAR, and Chandra, which are summarized in Table 1.

### 3.1. Suzaku

Suzaku ([Mitsuda et al. 2007](#)), the fifth Japanese X-ray astronomical satellite, observed the Circinus galaxy

**Table 1.** Summary of Observations

Observatory	ObsID	Date	Exposure
(1)	(2)	(3)	(4)
Chandra HETG	374	2000 June 15	7.26
Chandra HETG	62877	2000 June 16	61.4
Chandra HETG	4770	2004 June 2	56.1
Chandra HETG	4771	2004 Nov 28	60.2
Suzaku	701036010	2006 Jul 21	108 <sup>a</sup>
Chandra HETG	10226	2008 Dec 8	20.1
Chandra HETG	10223	2008 Dec 15	105
Chandra HETG	10832	2008 Dec 19	21.1
Chandra HETG	10833	2008 Dec 22	29.0
Chandra HETG	10224	2008 Dec 23	78.7
Chandra HETG	10844	2008 Dec 24	27.7
Chandra HETG	10225	2008 Dec 26	69.3
Chandra HETG	10842	2008 Dec 27	37.5
Chandra HETG	10843	2008 Dec 29	58.2
Chandra ACIS-S <sup>b</sup>	12823	2010 Dec 17	154
XMM-Newton	0701981001	2013 Feb 3	58.9
NuSTAR	60002039002	2013 Jan 25	53.9

NOTE— Column (1): observatory. Column (2): observation ID. Column (3): observation start date. Column (4): exposure time in units of ks.

<sup>a</sup> Based on the good time interval of an XIS camera with the shortest exposure among all XISs.

<sup>b</sup> Non grating observation.

in 2006 July. Analysis results utilizing these data were published in Yang et al. (2009), Arévalo et al. (2014), and Tanimoto et al. (2019), although Arévalo et al. (2014) did not include them in the spectral fitting. Suzaku carried four X-ray CCD cameras (X-ray Imaging Spectrometer, XIS: Koyama et al. 2007) and a collimated hard X-ray instrument (Hard X-ray Detector, HXD: Takahashi et al. 2007). XIS0, XIS2, and XIS3 are frontside-illuminated CCDs (XIS-FI: 0.4–12.0 keV) and XIS1 is a backside-illuminated one (XIS-BI: 0.2–12.0 keV). The HXD consists of two types of detectors: a GSO/BGO phoswich counter and PIN silicon diodes (Kokubun et al. 2007). The GSO/BGO counter is sensitive to 40–600 keV and PIN diodes to 10–70 keV. We analyzed the data using HEASoft v6.27 and the calibration database (CALDB) released on 2018 October 23 (XIS) and 2011 September 15 (HXD).

We reprocessed the unfiltered XIS data with the AEPIPELINE script. Events were extracted from a circular region with a radius of 100'' centered at the source

peak. We took the background from a source-free circular region with a radius of 100''. We generated the XIS redistribution matrix files (RMF) and ancillary response files (ARF) by using XISRMPGEN and XISSIMARFGEN, respectively. To improve the statistics, we combined the spectra of XIS-FI detectors (XIS0, XIS2, and XIS3) with ADDASCASPEC. We binned the XIS spectra to contain at least 100 counts per bin.

The unfiltered HXD data were also reprocessed with the AEPIPELINE script. We generated the PIN and GSO spectra by using HXD PINXBPI and HXD GSOXBPI, respectively. We utilized the tuned background files (Fukazawa et al. 2009) to obtain the non-X-ray background (NXB). The cosmic X-ray background (CXB) was added to the NXB of the PIN spectrum. The CXB in the GSO spectrum was ignored.

### 3.2. XMM-Newton

XMM-Newton (Jansen et al. 2001), the second ESA X-ray astronomical satellite, observed the Circinus galaxy six times between 2001 and 2018 (Molendi et al. 2003, Massaro et al. 2006, Arévalo et al. 2014, Tanimoto et al. 2019). In this paper, we utilize the data in 2013 February, which were taken simultaneously with NuSTAR (see below). XMM-Newton carries three X-ray CCD cameras: EPIC/pn (Strüder et al. 2001) and two EPIC/MOSs (Turner et al. 2001). We analyzed only the data of pn, which has the largest effective area, using the science analysis software (SAS) v18.0.0 and CALDB released on 2019 November 28.

We reprocessed the unfiltered pn data with the EP-PROC script. Source events were extracted from a circular region with a radius of 100'' centered at the source peak, for consistency with the Suzaku spectra. We subtracted the background taken from a source-free circular region with a radius of 100''. We generated the ARF and RMF by using ARFGEN and RMFGEN, respectively. We binned the pn spectrum to contain at least 100 counts per bin.

### 3.3. NuSTAR

NuSTAR (Harrison et al. 2013), the first X-ray astronomical satellite capable of focusing hard X-rays above 10 keV, observed the Circinus galaxy four times in 2013. The results were published in Arévalo et al. (2014), Brightman et al. (2015), and Tanimoto et al. (2019). NuSTAR carries two focal plane modules (FPMs), which are sensitive to 3–79 keV. We utilized the data observed in 2013 January, which are the only data observed on-axis. We used HEASoft v6.27 and CALDB released on 2020 May 14 for data reduction.

We reprocessed the FPMs data by using NUPIPELINE and NUPRODUCTS. Events were extracted from a circu-

lar region with a radius of  $100''$  centered at the source peak, and we subtracted the background taken from a source-free circular region with a radius of  $100''$ . We binned the FPMs spectra to contain at least 100 counts per bin.

### 3.4. *Chandra*

Chandra (Weisskopf et al. 2002) observed the Circinus galaxy several times since 2000 with the Advanced CCD Imaging Spectrometer (ACIS: Garmire et al. 2003) with or without the High Energy Transmission Grating (HETG: Canizares et al. 2005). Many authors published papers using a part of these data (with HETG: Sambruna et al. 2001; Bianchi et al. 2002; Shu et al. 2010; Shu et al. 2011; Arévalo et al. 2014; Liu 2016a,b; Hikitani et al. 2018; Kawamuro et al. 2019; without HETG: Marinucci et al. 2013; Arévalo et al. 2014, Kawamuro et al. 2019). Its excellent angular resolution ( $<1''$ ) enables us to separate the AGN from nearby X-ray sources by utilizing the ACIS imaging data. We analyzed 14 observations (13 with HETG and 1 without HETG). We followed the standard analysis procedures with the Chandra interactive analysis of observations (CIAO v4.12) software and calibration files (CALDB v4.9.1).

#### 3.4.1. *HETG Data*

Since our main purpose is to measure the width of the Fe  $K\alpha$  line, it is essential to fully utilize the available Chandra/HETG data, which achieve the best energy resolution in the iron-K band among existing missions. We analyzed the data of the whole 13 observations, whose summed net exposure amounted to 0.62 Ms. Source events were extracted from  $4.8''$  full-width HEG regions in the cross-dispersion direction centered at the AGN. The background was extracted from both sides of the source extraction region by carefully selecting areas not containing the two bright sources: CGX1 and CGX2 (see Section 3.4.2). We combined the spectra from all the observations. To perform  $\chi^2$  minimization simultaneously with the other spectra, the first order HEG spectrum was binned to contain at least 50 counts per bin.

#### 3.4.2. *ACIS Imaging Data*

The X-ray image of the Circinus galaxy is complex and is extended over a few arcmins, consisting of the AGN core, point-like sources, and diffuse emission (Yang et al. 2009, Marinucci et al. 2013, Arévalo et al. 2014, Kawamuro et al. 2019). Hence, the Suzaku, XMM-Newton, and NuSTAR spectra taken with a large aperture ( $100''$ ) contain all these components. To estimate the contribution from the contaminating sources near the AGN

in these spectra, we re-analyzed the imaging data observed with ACIS-S without HETG in 2010 December. We extracted the spectra of CGX1 (ultraluminous X-ray source; ULX) and CGX2 (supernova remnant; SNR) from circular regions with radii of  $3''$  centered at the source peaks. We subtracted the backgrounds taken from annuli with inner and outer radii of  $3''$  and  $4''$  surrounding the sources. There are also dimmer point sources and diffuse emission around the AGN. We extracted their integrated spectrum (we hereafter refer to it as “diffuse spectrum”) from a circular region with a radius of  $100''$  centered at the AGN by masking the three regions with radii of  $3''$  centered at the AGN, CGX1, and CGX2. We binned the CGX1, CGX2, and diffuse spectra to contain at least 50, 30 and 100 counts per bin, respectively.

## 4. SPECTRAL ANALYSIS AND RESULTS

We first evaluate the contribution of the contaminating sources with the Chandra imaging data, basically following Arévalo et al. (2014) with revisions. Then, we perform a simultaneous fit to the 3–100 keV spectra of the Circinus galaxy observed with Suzaku, XMM-Newton, NuSTAR, and Chandra/HETG, in order to best determine the broadband spectral model of the AGN. Finally, we perform a detailed analysis of the Fe  $K\alpha$  line profile with the Chandra/HETG spectra of different grating orders, where we take into account the effect of spatial extent. In the spectral fit, we always multiply the Galactic absorption, modelled by *phabs* in XSPEC (Arnaud 1996), to the spectral models of the AGN and galaxy emission. Its hydrogen column density is fixed at  $7.02 \times 10^{21} \text{ cm}^{-2}$ , a value estimated by the method of Willingale et al. (2013).

### 4.1. *Contamination*

#### 4.1.1. *CGX1*

Qiu et al. (2019) showed that CGX1 was an ULX. Here we adopt a spectral model developed by Shidatsu et al. (2017), a physically motivated model that well reproduces broadband spectra of a ULX covering the hard X-ray band above 10 keV. This model consists of two components: disk blackbody radiation from the accretion disk and Comptonization in the optically thick corona. The seed photon temperature of the Comptonized component ( $T_0$ ) is set to be twice that of the disk innermost temperature ( $T_{\text{in}}$ ) (see Shidatsu et al. 2017 for details). The model is represented as follows in the XSPEC terminology:

$$\text{CGX1} = \text{phabs}*(\text{diskbb}+\text{mscomptt}), \quad (3)$$

where *mscomptt* is a local model by Shidatsu et al. (2017). We obtain a good fit with the model ( $\chi^2_{\text{red}} =$

175/161). Table 2 summarizes the best-fit parameters. Figure 2 shows the X-ray spectrum folded with the energy response and the best-fit model.

#### 4.1.2. CGX2

To model the spectrum of CGX2, an SNR, we use basically the same model as that in Arévalo et al. (2014), which consists of three components of optically-thin thermal plasma. The model is represented as follows in the XSPEC terminology:

$$\text{CGX2} = \text{phabs} \quad (4)$$

$$* \{ \text{apec1} + \text{apec2} + \text{gsmooth}(0.065 \text{ keV}) * \text{apec3} \}$$

Here we employ the `apec` model instead of `mekal` adopted by Arévalo et al. (2014) because the latter does not cover the energy band above  $\sim 50$  keV. We confirm that it successfully reproduces the spectrum ( $\chi_{\text{red}}^2 = 308/270$ ). Table 3 summarizes the best fit parameters. Figure 3 shows the folded X-ray spectrum and the best-fit models.

#### 4.1.3. Diffuse Emission

The diffuse emission is mainly originated from X-ray reflection by gas around the nucleus of the intrinsic AGN emission. Accordingly, we adopt `pexmon` (Magdziarz & Zdziarski 1995), a Compton reflection model from optically thick matter, and a scattered component by optically thin matter (cutoff power-law), to reproduce the spectrum. We also add emission lines reported in Arévalo et al. (2014) that are not included in the `pexmon` model (Table 5). The model is represented as follows in the XSPEC terminology:

$$\text{diffuse} = \text{phabs} * (\text{pexmon} + \text{zcutoffpl} + \text{zgausses}) \quad (5)$$

We link the photon index and cutoff energy to those of the intrinsic AGN component in the simultaneous fitting of the broadband spectra (see Section 4.2.1). The inclination angle in the `pexmon` model is fixed at  $60^\circ$ .

### 4.2. Broadband Spectral Fitting

#### 4.2.1. Spectral Models

Earlier works showed that many high-order ionization lines were present in the spectrum of the Circinus galaxy below 3 keV (e.g., Sambruna et al. 2001). This suggests that the soft band is characterized by significant emission from photoionized plasma. To focus on the reflection component from the torus, we ignore the data below 3 keV. We perform simultaneous fits to the spectra observed with Chandra/HETG (HEG first order, 3–8 keV), Chandra/ACIS (imaging, 3–7 keV),

Suzaku/XIS-FI (3–10 keV), Suzaku/XIS-BI (3–10 keV), Suzaku/PIN (20–40 keV), Suzaku/GSO (50–100 keV), XMM-Newton/pn (3–10 keV), NuSTAR/FPMA (8–70 keV), and NuSTAR/FPMB (8–70 keV).

The X-ray spectrum of an obscured AGN mainly consists of three components: a transmitted component, a reflection component from the torus, and an unabsorbed scattered component (e.g., Kawamuro et al. 2016, Tanimoto et al. 2018). We accordingly model the emission from the AGN (not including the diffuse component mentioned in Section 4.1) as follows in the XSPEC terminology:

$$\text{AGN} = \text{phabs}$$

$$* (\text{zvphabs} * \text{cabs} * \text{zcutoffpl} + \text{const1} * \text{zcutoffpl}$$

$$+ \text{atable}\{\text{xclumpyv\_R.fits}\}$$

$$+ \text{const2} * \text{atable}\{\text{xclumpyvd\_L.fits}\}$$

$$+ \text{zgausses}) \quad (6)$$

1. The first term (`phabs`) represents the Galactic absorption.
2. The first term in the parentheses represents the transmitted component through the torus. The `zvphabs` and `cabs` models represent photo-electric absorption and Compton scattering by the torus, respectively.
3. The second term in the parentheses represents the unabsorbed scattered component. The parameters of `zcutoffpl` (photon index, cutoff energy, normalization) are linked to those of the transmitted component. The `const1` factor gives the scattering fraction.
4. The third and fourth terms in the parentheses represent the reflection continuum and the fluorescence lines from the torus. The metal abundance, photon index, cutoff energy, and normalization are set to those of the transmitted component. We introduce a relative normalization factor of the emission lines to the reflection continuum (`const2`) to take into account systematic uncertainties due to the simplified assumption of the torus geometry.
5. We add the emission lines reported by Arévalo et al. (2014) not included in the XCLUMPY model (Table 5).

The whole model used for the simultaneous fitting is represented as follows:

$$\text{model1} = \text{const3} * \text{AGN}$$

$$\text{model2} = \text{const3} * \text{diffuse}$$

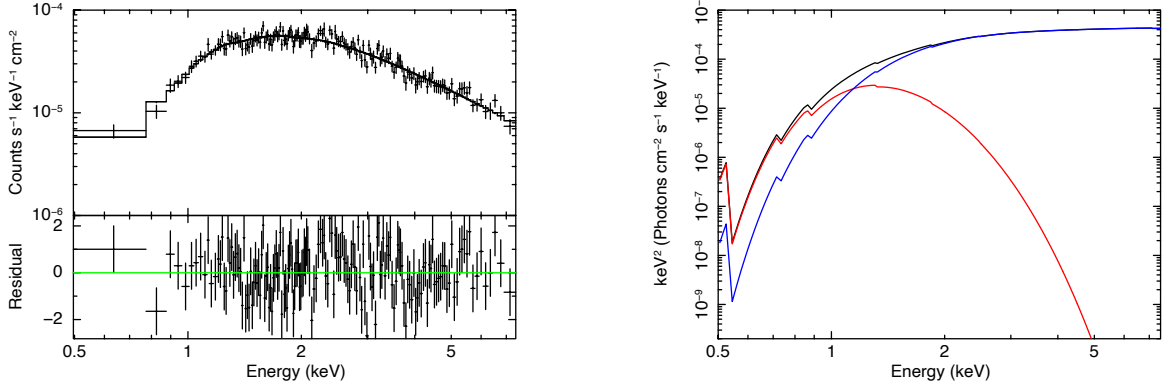


**Figure 2.** (Left) The folded spectrum of CGX1 obtained with Chandra/ACIS. The lower panel shows the fitting residuals. (Right) The best-fit models. The black, blue, and red lines represent the total component, the Comptonized component, and the disk black body component, respectively.

**Table 2.** Best Fit Parameters of CGX1

$N_{\text{H}}$	$kT_{\text{in}}$	$N_{\text{dbb}}$	$z$	$kT_0/kT_{\text{in}}$	$kT_e$	$\tau$	$N_{\text{mscomptt}}$	$F_{2-10}$	$\chi^2/\text{dof}$
(1)	(2)	(3)	(4)	(5)	(6)	(7)	(8)	(9)	
$1.07^{+0.21}_{-0.19}$	$0.21^{+0.04}_{-0.04}$	$29.6^{+70.4a}_{-20.3}$	0.0014 (fixed)	2.0 (fixed)	4.0 (fixed)	$5.03^{+0.26}_{-0.30}$	$(1.02^{+0.16}_{-0.11}) \times 10^{-4}$	$9.7 \times 10^{-13}$	175/161

NOTE— Column (1): hydrogen column density in units of  $10^{22}$  atoms  $\text{cm}^{-2}$ . Column (2): innermost temperature of the disk. Column (3): normalization of diskbb. Column (4): redshift fixed at that of the Circinus galaxy. Column (5): ratio of the seed-photon temperature ( $T_0$ ) to the disk innermost temperature ( $T_{\text{in}}$ ). Column (6): plasma temperature in units of keV. Column (7): Thomson scattering optical depth. Column (8): normalization of mscomptt. Column (9): observed X-ray flux in the 2–10 keV band in units of  $\text{erg cm}^{-2} \text{s}^{-1}$ .

<sup>a</sup>The parameter reaches a limit of its allowed range.

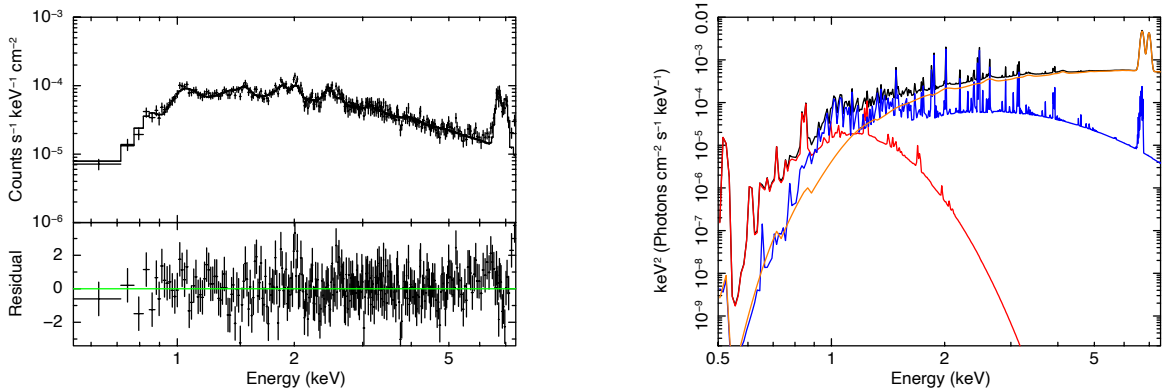


**Figure 3.** (Left) The folded spectrum of CGX2 observed with Chandra/ACIS. The lower panel shows the fitting residuals. (Right) The best-fit models. The black line represents the total spectrum. The red, blue, and orange lines correspond to the three components of optically-thin thermal emission in descending order of temperature.

$$\text{model3} = \text{const3} * (\text{AGN} + \text{diffuse} + \text{const4} * \text{CGX1} + \text{CGX2}) \quad (7)$$

1. The model forms of ‘CGX1’, ‘CGX2’, ‘diffuse’ and ‘AGN’ are described in Equations (3)-(6), respec-

**Table 3.** Best Fit Parameters of CGX2

Model	$N_{\text{H}}$ ( $10^{22}$ )	$kT$ (keV)	$Z$	$z$	Norm.
phabs	$1.64^{+0.09}_{-0.05}$	...	...	...	...
apec1	...	$0.143^{+0.003}_{-0.012}$	0.5 (fixed)	$(8.28^{+0.20}_{-1.25}) \times 10^{-2}$	$(1.75^{+1.24}_{-0.65}) \times 10^{-1}$
apec2	...	$1.15^{+0.05}_{-0.05}$	$5.0^{+0.9}_{-0.6}$	$(-5.65^{+0.70}_{-8.58}) \times 10^{-3}$	$(2.16^{+0.39}_{-0.10}) \times 10^{-4}$
apec3	...	$9.88^{+0.71}_{-0.73}$	5.0 (linked)	$(-2.63^{+0.15}_{-0.44}) \times 10^{-3}$	$(6.42^{+0.15}_{-0.49}) \times 10^{-4}$

NOTE— The metal abundance of the lowest temperature component is fixed at 0.5. Those of the high and medium temperature components are linked together.

tively. The parameters of CGX1 and CGX2 were frozen at the best-fit values obtained by the spectral analysis of the Chandra/ACIS imaging data (Section 4.1). As mentioned above, the photon index and cutoff energy of the diffuse component are linked to those of the AGN one.

- We apply model1 to the Chandra/HETG spectrum, model2 to the Chandra/ACIS diffuse spectrum, and model3 to the other spectra.
- The `const3` is a cross-normalization factor to correct for a possible difference in the absolute flux calibration among different instruments. We fix that of Chandra/HETG at unity as a reference. Those of Suzaku/XIS-FI ( $C_{\text{FI}}$ ), Suzaku/XIS-BI ( $C_{\text{BI}}$ ), XMM-Newton/pn ( $C_{\text{pn}}$ ), NuSTAR/FPMA ( $C_{\text{FPMA}}$ ) and NuSTAR/FPMB ( $C_{\text{FPMB}}$ ) are left as free parameters. Those of Suzaku/PIN and Suzaku/GSO are set to be  $1.16 \times C_{\text{FI}}$  based on the calibration with the Crab Nebula. The cross-normalization of Chandra/ACIS diffuse spectrum is fixed at unity.
- The `const4` accounts for time variability of the ULX (CGX1). Those of Suzaku/XIS-FI ( $T_{\text{FI}}$ ) and XMM-Newton/pn ( $T_{\text{pn}}$ ) are left as free parameters. Those of Suzaku/XIS-BI, Suzaku/PIN, and Suzaku/GSO are linked to  $T_{\text{FI}}$ , whereas those of NuSTAR/FPMA and NuSTAR/FPMB are to  $T_{\text{pn}}$  (because the NuSTAR and XMM-Newton observations were simultaneous). We note that the X-ray spectrum of a ULX changes with luminosity; generally, it becomes softer at higher luminosities (e.g., Walton et al. 2014; Shidatsu et al. 2017). Applying the same model adopted here to the spectra of IC 342 X-1 observed in multiple epochs, Shidatsu et al. (2017) obtained  $\sim 20\%$  smaller optical depths ( $\tau$ ) of the Comptonizing corona when the luminosity increased by a factor

of 2 – 3. Accordingly, we repeat our analysis by setting  $\tau = 4$  for the CGX1 spectra in the Suzaku and NuSTAR/XMM-Newton data, where its luminosity is estimated to be  $\sim 2$  higher than in the Chandra data (Table 4). We confirm that it has little effect on the result of our broadband spectral fitting of the Circinus galaxy because the luminosity of CGX1 is sufficiently small compared with that of the AGN. Thus, we adopt the result obtained by considering only the luminosity change of CGX1.

All the redshift parameters in the AGN and diffuse components are linked together for the spectrum of each instrument. Since the AGN contains a strong Fe  $K\alpha$  line, the redshift determination based on it very sensitively depends on the precise energy-scale calibration of each instrument; in fact, we find that adopting a common redshift value for all the instruments leads to highly unacceptable fits. (If we fix the redshifts of all instruments to 0.0014, we obtain even a much worse fit with  $\chi^2/\text{dof} = 2468/1996$ .) To take into account the possible calibration uncertainties in an approximated way, we allow the linked value of the redshift to vary among different instruments except for the Suzaku/HXD and NuSTAR spectra, for which we fix  $z = 0.0014$ . We confirm that the resultant redshift parameters are consistent with  $z = 0.0014$  within the calibration uncertainties (Chandra Calibration Status Summary<sup>3</sup>, Koyama et al. 2007, XMM-Newton Calibration Technical Note<sup>4</sup>). Note that, for simplicity, we have ignored these small scale uncertainties in modeling the CGX1 and CGX2 spectra because they do not affect our results on the AGN component.

<sup>3</sup> <https://cxc.cfa.harvard.edu/cal/summary/Calibration.Status.Report.html>

<sup>4</sup> <https://xmmweb.esac.esa.int/docs/documents/CAL-TN-0018.pdf>

#### 4.2.2. Results

We successfully reproduce the broadband (3–100 keV) spectra of the Circinus galaxy with the above model. The best-fit parameters are summarized in Table 4. Figure 4 shows the folded X-ray spectra and best-fit models. We obtain the main torus parameters  $N_{\text{H}}^{\text{Equ}} = 2.16_{-0.17}^{+0.24} \times 10^{25} \text{ cm}^{-2}$ ,  $\sigma = 10.3_{-0.3}^{+0.8}$  degrees, and  $i = 78.3_{-0.9}^{+0.5}$  degrees. We also find that the supersolar abundance ( $Z = 1.52_{-0.06}^{+0.05}$ ) significantly improve the fit, mainly to reproduce the Compton-shoulder fraction (see Appendix C). The cross-normalization factors of XMM-Newton/pn and Suzaku/XIS are consistent with Madsen et al. (2017) but those of NuSTAR/FPMs are not.<sup>5</sup> The best-fit value of `const2` (the relative normalization factor of line components to the continuum in XCLUMPY),  $1.08_{-0.05}^{+0.06}$ , is slightly over 1.0. Since the torus parameters, such as  $N_{\text{H}}^{\text{Equ}}$ , affect the equivalent width of the Fe K $\alpha$  line (see Figure 4 in Tanimoto et al. 2019), this may be explained if the actual distribution of clumps in the elevation direction is not perfectly represented by a single gaussian model as assumed (e.g., more material exists very close to the equatorial plane). Nevertheless, the result that `const2` is close to unity supports that the assumed geometry is a good approximation. The bolometric luminosity is estimated to be  $L_{\text{bol}} = 1.27_{-0.13}^{+0.09} \times 10^{44} \text{ erg s}^{-1}$  by assuming the relation of X-ray and bolometric luminosities of  $L_{\text{bol}} = 20 \times L_{2-10}$  (Vasudevan & Fabian 2009).<sup>6</sup> We compare these results with previous studies in Section 6.

## 5. DETAILED ANALYSIS OF FE K $\alpha$ LINE

### 5.1. Imaging Analysis

Marinucci et al. (2013) analyzed Chandra imaging data of the Circinus galaxy and detected a spatial extent of the Fe K $\alpha$  line emitting region. The spatial extent has line-broadening effects in grating spectra, which we have to correct for in order to accurately measure the intrinsic spectral line width.<sup>7</sup> In this subsection, we confirm the spatial extent of the Fe K $\alpha$  line emitting region by comparing the radial profile obtained from a Chandra image with that obtained from simulations. We analyze the 0th order image of ObsID = 4771, one of the longest exposure data with HETGs, which is little affected by pile-up thanks to the grating mode.

<sup>5</sup> We infer that, this is because Madsen et al. (2017) calibrated NuSTAR/FPMs in the 1–5 keV and 3–7 keV bands, whereas our cross-normalization factors are determined by using only the 8–10 keV band.

<sup>6</sup> The error is estimated by fixing the photon index at the best-fit value.

<sup>7</sup> [https://cxc.harvard.edu/newsletters/news\\_24/](https://cxc.harvard.edu/newsletters/news_24/)

We perform simulations with the MARX code (Davis et al. 2012), which produces simulated event files based on a Monte-Carlo method. The input spectrum is determined from our broadband spectral fitting in Section 4. Since the `AspectBlur` parameter in MARX is still under calibration, we perform simulations with two different settings, `AspectBlur=0.0''` and `0.25''`, referring to Fabiano et al. (2020) and the latest PSF calibration by the MARX team<sup>8</sup>, respectively. Figure 5 compares the simulated and observed source radial profiles. This confirms that the Circinus galaxy has a spatial extent in the 6.0–7.0 keV band regardless of the adopted value of `AspectBlur`. Note that the extent is not circularly symmetric but has a complex structure (Marinucci et al. 2013). Hence, we cannot refer to this plot to estimate the extent along the dispersion direction of the HEG data in a given observation.

### 5.2. Spectral Analysis

Since the width of the line-broadening effect due to a spatial extent is inversely proportional to the grating order (Appendix A), in principle, we can separate the effect by simultaneously analyzing multiple spectra of different grating orders. Thus, we perform a simultaneous fitting to the Chandra/HETG first, second, and third order spectra in the 6.3–6.5 keV band. Considering the small photon statistics, we bin each spectrum to contain at least one count per bin, and use Cash statistics (Cash; Cash 1979) to determine the best-fit parameters. We use basically the same model as `model1` (Equation 7) but take into account the line broadening effect by the spatial extent, which is proportional to the inverse of the grating order (see Appendix A). The model is represented as follows in the XSPEC terminology:

$$\begin{aligned} \text{model4} = & \text{const3*phabs} \\ & * (\text{zvphabs*cabs*zcutoffpl} + \text{const1*zcutoffpl} \\ & + \text{atable}\{\text{xclumpyv\_R.fits}\} \\ & + (1-\text{const5})*\text{atable}\{\text{xclumpyvd\_L.fits}\} \\ & + \text{const5*gsmooth}*\text{atable}\{\text{xclumpyvd\_L.fits}\} \\ & + \text{zgausses} \end{aligned} \quad (8)$$

1. The `const5` represents the fraction of the extended emission in the total intensity ( $f_{\text{diff}}$ ), which is left as a free parameter.

2. The 4th and 5th terms correspond to the fluorescence lines from the point-like and extended regions. The `gsmooth` model represents the spatial

<sup>8</sup> <https://cxc.cfa.harvard.edu/ciao/why/aspectblur.html>

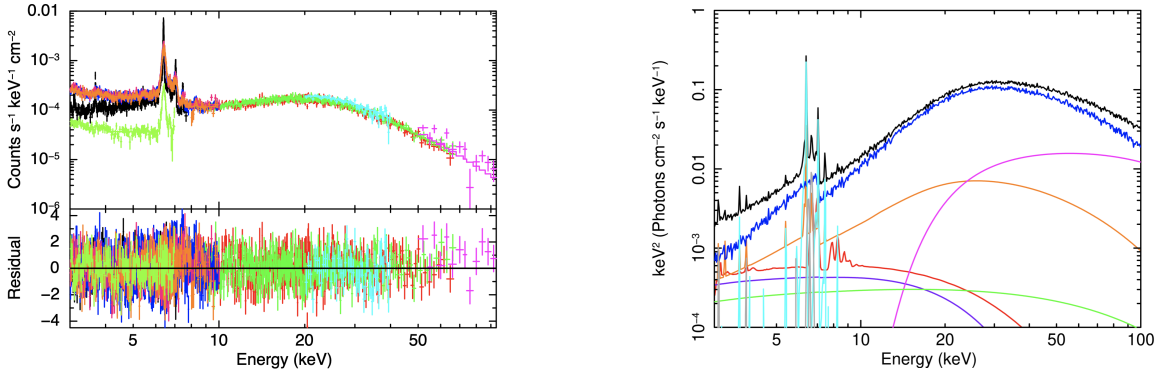


**Figure 4.** (Left) The folded spectra of the Circinus galaxy. Black: Chandra/HETG. Blue: Suzaku/XIS-FI. Dark red: Suzaku/XIS-BI. Light blue; Suzaku/PIN. Magenta: Suzaku/GSO. Orange: XMM-Newton/PN. Red: NuSTAR/FPMA. Green: NuSTAR/FPMB. Light green: Chandra/ACIS. (Right) Black: total. Magenta: direct component. Green: scattered component. Blue: reflection continuum of the updated XCLUMPY model (xclumpyv.R.fits). Light Blue: fluorescence lines of the updated XCLUMPY model (xclumpyvd.L.fits), Orange: diffuse contamination. Purple: CGX1. Red: CGX2. Gray: added emission lines. The noises noticeable in the reflection continuum model are due to the statistic fluctuation in the simulated spectra, which have negligible effects on the fitting.

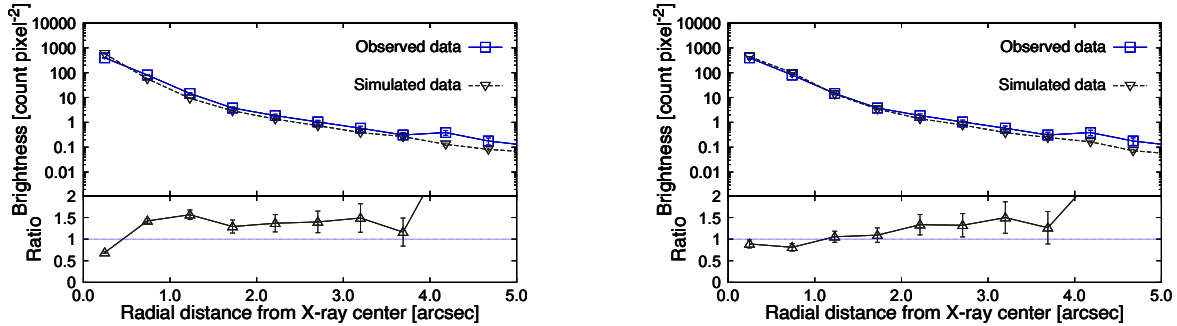


**Figure 5.** Comparisons of the radial profile in the 6–7 keV band between the observed data and simulation. (left) AspectBlur=0.00'' (right) AspectBlur=0.25''

broadening effect. Its width is left as a free parameter ( $\sigma_{\text{E}}^{\text{diff}}$ ). The torus inner radius in the 4th term is left free, whereas that in the 5th one is fixed at  $\log(r_{\text{in}}/r_{\text{g}}) = 7.0$  (i.e., effectively no intrinsic spectral broadening).

3. The cross-normalization factors (const3) of the second and third order spectra are left as free parameters, whereas that of the first order one is fixed at unity. The normalization of the lines (xclumpyvd.L.fits) and the torus inner radius ( $r_{\text{in}}/r_{\text{g}}$ ) are set free. The other parameters are fixed to the values in Tables 4 and 5.

The best-fit parameters are summarized in Table 6. Figure 6 shows the folded X-ray spectra and the best-fit models. We estimate the inner radius of the torus to be  $\log(r_{\text{in}}/r_{\text{g}}) = 5.28^{+0.42}_{-0.23}$ . Since the mass of the SMBH is  $(1.7 \pm 0.3) \times 10^6 M_{\odot}$  (Greenhill et al. 2003), it corresponds to  $r_{\text{in}} = 1.6^{+1.5}_{-0.9} \times 10^{-2}$  pc. At the same time, the

spectral analysis also constrains the spatial extent of Fe  $K\alpha$  in the Circinus galaxy averaged over the dispersion directions of the whole HEG data used in our analysis: the fraction of the extended emission is  $0.19^{+0.16}_{-0.09}$  and the angular width is  $\sigma_{\text{angl}}^{\text{diff}} = 0.66^{+0.33}_{-0.21}$  arcsec.

## 6. DISCUSSION

We have updated the XCLUMPY model by incorporating two new features: variable metal abundance and Doppler effects due to a Keplerian motion of each clump. Using this model, we have analyzed currently the best available broadband (3–100 keV) X-ray spectra of the Circinus galaxy observed with Suzaku, XMM-Newton, NuSTAR and Chandra, including deep Chandra/HETG data of 0.62 Ms. These rich datasets, together with the state-of-art reflection model from an AGN torus, have enabled us to best determine the shape of the broadband spectrum and Fe  $K\alpha$  line profile of the Circinus

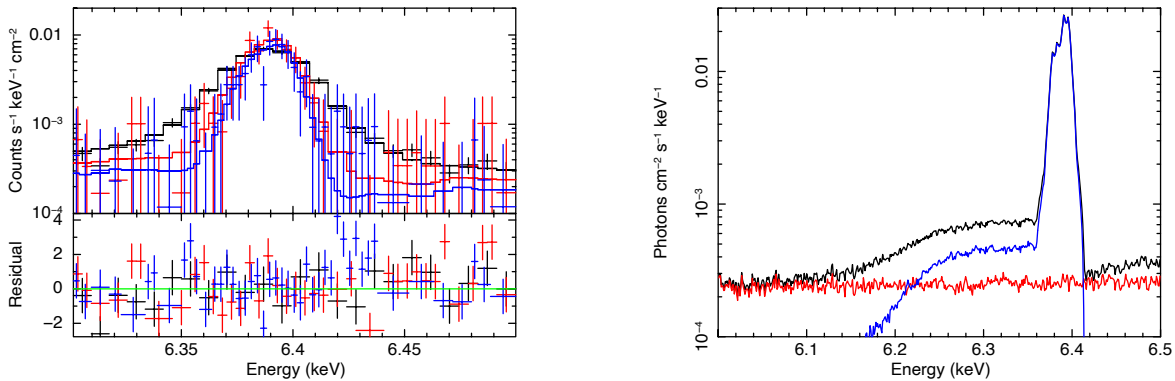


**Figure 6.** (Left) The folded spectra and fitting residuals around the Fe K $\alpha$  line. Black: Chandra/HETG first order spectrum. Red: second order. Blue: third order. (Right) The best-fit models. The black, red, and blue lines represent the total component, the continuum, and the Fe K $\alpha$  line, respectively.

galaxy. Below, we discuss our results focusing on the torus properties.

### 6.1. Broadband Spectra

We confirm the previous results based on broadband X-ray spectroscopy (e.g., Arévalo et al. 2014; Tanimoto et al. 2019) that the AGN torus in the Circinus galaxy is Compton-thick ( $N_{\text{H}}^{\text{Equ}} = 2.16^{+0.24}_{-0.17} \times 10^{25} \text{ cm}^{-2}$ ;  $N_{\text{H}}^{\text{LOS}} = 5.95^{+0.76}_{-0.60} \times 10^{24} \text{ cm}^{-2}$ ), geometrically thin ( $\sigma = 10.3^{+0.8}_{-0.3}$  degrees), and viewed edge-on ( $i = 78.3^{+0.5}_{-0.9}$  degrees). Our results supercede the earlier work by Tanimoto et al. (2019), who first applied XCLUMPY to the broadband spectrum of the Circinus galaxy observed with Suzaku, XMM-Newton, and NuSTAR. They obtained  $N_{\text{H}}^{\text{Equ}} = 9.08^{+0.14}_{-0.08} \times 10^{24} \text{ cm}^{-2}$  ( $N_{\text{H}}^{\text{LOS}} = 4.86^{+0.07}_{-0.04} \times 10^{24} \text{ cm}^{-2}$ ),  $\sigma = 14.7^{+0.5}_{-0.4}$  degrees,  $i = 78.3^{+0.2}_{-0.2}$  degrees. Our inclination angle is consistent with the Tanimoto et al. (2019) value, whereas the hydrogen column density along the equatorial plane and torus angular width are somewhat larger and smaller than theirs, respectively. We infer that the differences arise because Tanimoto et al. (2019) assumed the solar abundance and did not separately treat the diffuse emission, which contaminates the AGN spectrum in a soft band. In Tanimoto et al. (2019) these effects worked to overestimate the photon index of the intrinsic power-law component ( $\Gamma = 1.80^{+0.01}_{-0.03}$  compared with our result of  $\Gamma = 1.68^{+0.05}_{-0.09}$ ) and hence required a larger solid angle of the reflector (i.e., a larger torus angular width) to reproduce the observed reflection spectrum. Since the column density along the line of sight ( $N_{\text{H}}^{\text{LOS}}$ ) is well constrained by the spectrum, the large torus angular width may have led them to underestimate that along the equatorial plane ( $N_{\text{H}}^{\text{Equ}}$ ).

Arévalo et al. (2014) analyzed the XMM-Newton and NuSTAR data of the Circinus galaxy observed in 2013 with the MYTorus and Torus models, and obtained  $N_{\text{H}}^{\text{Equ}} = 6.6\text{--}10 \times 10^{24} \text{ cm}^{-2}$ ,  $\Gamma = 2.2\text{--}2.4$ . Our hydrogen column density along the equatorial plane ( $N_{\text{H}}^{\text{Equ}} = 21.6^{+2.4}_{-1.7} \times 10^{24} \text{ cm}^{-2}$ ) and photon index ( $\Gamma = 1.68^{+0.05}_{-0.09}$ ) are larger and smaller than their results, respectively. As mentioned in Tanimoto et al. (2019), we infer that because the XCLUMPY model contains a larger flux of the unabsorbed reflection component, it leads to a flatter intrinsic spectrum. Also, the differences in the adopted torus geometry inevitably affect the estimate of  $N_{\text{H}}^{\text{Equ}}$ . We refer the reader to Tanimoto et al. (2019) for detailed comparison of spectral analysis results between the XCLUMPY model and other torus models.

Our result that the metal abundance is super-solar ( $Z = 1.52^{+0.05}_{-0.06}$ ) is consistent with Molendi et al. (2003), who estimated the iron abundance to be 1.2–1.7 solar from the Fe K $\alpha$  edge. As mentioned in Section 1, Hikitani et al. (2018) derived  $Z \approx 1.75$  from the Compton shoulder of the Fe K $\alpha$  line utilizing a torus model developed by Furui et al. (2016). Our result is slightly smaller than their result, which was based on a more geometrically-thick torus model.

According to our best-fit parameters of XCLUMPY, the expected number of clumps along the line of sight is  $\sim 3$ . The hydrogen number density of each clump ( $n_{\text{H}}$ ) can be calculated with Equation 9 (see also Equation 5 in Tanimoto et al. 2019). In our case,  $n_{\text{H}} = 8.2 \times 10^8 \text{ cm}^{-3}$ , which is almost consistent with those estimated by Markowitz et al. (2014) for nearby Seyfert galaxies.

$$n_{\text{H}} = \frac{3N_{\text{H}}^{\text{Equ}}}{40R_{\text{clump}}} \quad (9)$$

**Table 4.** Best Fit Parameters of the Broadband Spectra

Region	No.	Parameter	Best Fit Value	Units
AGN	(1)	$N_{\text{H}}^{\text{Equ}}$	$21.6^{+2.4}_{-1.7}$	$10^{24} \text{ cm}^{-2}$
	(2)	$N_{\text{H}}^{\text{LOS}}$	$5.95^{+0.76}_{-0.60}$	$10^{24} \text{ cm}^{-2}$
	(3)	$Z$	$1.52^{+0.05}_{-0.06}$	solar value
	(4)	$\sigma$	$10.3^{+0.8}_{-0.3a}$	degree
	(5)	$i$	$78.3^{+0.5}_{-0.9}$	degree
	(6)	$\Gamma$	$1.68^{+0.05}_{-0.09}$	
	(7)	$E_{\text{cut}}$	$48.0^{+5.0}_{-5.4}$	keV
	(8)	$N_{\text{Line}}$	$1.08^{+0.06}_{-0.05}$	
	(9)	$\log(r_{\text{in}}/r_{\text{g}})$	$4.84^{+0.08}_{-0.08}$	
	(10)	$N_{\text{Dir}}$	$0.80^{+0.11}_{-0.18}$	photons $\text{keV}^{-1} \text{ cm}^{-2} \text{ s}^{-1}$
	(11)	$f_{\text{scat}}$	$2.2^{+1.8}_{-1.1} \times 10^{-2}$	%
	(12)	$L_{2-10}$	$6.34^{+0.43}_{-0.64}$	$10^{42} \text{ ergs}^{-1}$
diffuse	(13)	$Z$	$0.96^{+0.12}_{-0.11}$	solar value
	(14)	$N_{\text{pexmon}}$	$6.75^{+0.90}_{-1.22} \times 10^{-3}$	photons $\text{keV}^{-1} \text{ cm}^{-2} \text{ s}^{-1}$
	(15)	$N_{\text{zcutoffpl}}$	$2.14^{+0.47}_{-0.47} \times 10^{-4}$	photons $\text{keV}^{-1} \text{ cm}^{-2} \text{ s}^{-1}$
	(16)	$C_{\text{FI}}$	$0.85^{+0.02}_{-0.02}$	
	(17)	$C_{\text{BI}}$	$0.90^{+0.03}_{-0.03}$	
	(18)	$C_{\text{pn}}$	$0.81^{+0.03}_{-0.03}$	
	(19)	$C_{\text{FPMA}}$	$0.80^{+0.03}_{-0.03}$	
	(20)	$C_{\text{FPMB}}$	$0.83^{+0.03}_{-0.03}$	
	(21)	$T_{\text{FI}}$	$1.88^{+0.30}_{-0.30}$	
	(22)	$T_{\text{pn}}$	$2.29^{+0.39}_{-0.39}$	
	(23)	$z_{\text{HETG}}$	$1.64^{+0.10}_{-0.09} \times 10^{-3}$	
	(24)	$z_{\text{FI}}$	$0.70^{+0.22}_{-0.22} \times 10^{-3}$	
	(25)	$z_{\text{BI}}$	$-0.33^{+0.39}_{-0.41} \times 10^{-3}$	
	(26)	$z_{\text{pn}}$	$-1.41^{+0.46}_{-0.47} \times 10^{-3}$	
	(27)	$z_{\text{ACIS}}$	$-0.72^{+0.88}_{-1.01} \times 10^{-3}$	
	(28)	$F_{2-10}$	$1.39 \times 10^{-11}$	$\text{erg cm}^{-2} \text{ s}^{-1}$
	(29)	$F_{10-100}$	$2.62 \times 10^{-10}$	$\text{erg cm}^{-2} \text{ s}^{-1}$
		$\chi^2/\text{dof}$	2275/1991	

NOTE— (1) Hydrogen column density along the equatorial plane. (2) Hydrogen column density along the line of sight. (3) Metal abundance of the torus. (4) Torus angular width. (5) Inclination angle. (6) Photon index. (7) Cutoff energy. (8) Relative normalization of the emission lines to the reflection continuum. (9) Torus inner radius in units of gravitational radius. (10) Normalization of the direct component. (11) Scattering fraction in percent. (12) Intrinsic AGN luminosity in the 2–10 keV band. (13) Metal abundance of the diffuse emission. Iron abundance was set to this value. (14) Normalization of the reflection component in the diffuse emission. (15) Normalization of the scattered component in the diffuse emission. (16)–(20) Cross-normalization factors. (21)–(22) Time-variability factors. (23)–(27) Redshift of each spectrum. Those of NuSTAR and Suzaku/HXD are fixed at 0.0014. (28)–(29) Obscured AGN flux in the 2–10 keV and 10–100 keV band.

<sup>a</sup>The parameter reaches a limit of its allowed range.

**Table 5.** Emission Lines Added in the Model

Region	Energy (keV)	Sigma (eV)	Norm. (photons cm <sup>-2</sup> s <sup>-1</sup> )	ID
(1)	(2)	(3)	(4)	(5)
AGN	3.11	5.8	$3.9^{+1.4}_{-1.3} \times 10^{-6}$	S <sub>XVI</sub> K $\beta$
	3.90	4.8	$1.68^{+0.87}_{-0.87} \times 10^{-6}$	Ar <sub>XVIII</sub>
	5.88	1.0	$0.89^{+1.18}_{-0.89} \times 10^{-6}$ <sup>a</sup>	Cr <sub>XXIV</sub>
	6.50	50.0	$1.41^{+0.48}_{-0.51} \times 10^{-5}$	Fe <sub>XX</sub>
	$6.68^{+0.01}_{-0.01}$	$50.6^{+17.5}_{-12.9}$	$2.86^{+0.46}_{-0.40} \times 10^{-5}$	Fe <sub>XXV</sub>
diffuse	3.11	5.8	$2.8^{+1.2}_{-1.2} \times 10^{-6}$	S <sub>XVI</sub> K $\beta$
	3.27	1.2	$2.16^{+1.02}_{-1.02} \times 10^{-6}$	Ar <sub>XVIII</sub>
	3.69	1.0	$1.44^{+0.89}_{-0.94} \times 10^{-6}$	Ca <sub>II-XIV</sub> + Ar <sub>XVII</sub>
	3.90	4.8	$1.57^{+0.85}_{-0.88} \times 10^{-6}$	Ar <sub>XVIII</sub>
	5.41	0.1	$1.49^{+0.99}_{-1.01} \times 10^{-6}$	Cr <sub>I</sub>
	6.68(linked)	10.0	$4.9^{+2.4}_{-2.4} \times 10^{-6}$	Fe <sub>XXV</sub>

NOTE— Column (1): region. Column (2): line energy. These are fixed at the values reported in [Arévalo et al. \(2014\)](#) except for Fe<sub>XXV</sub> line. It is allowed to vary within 50 eV centered at 6.66 keV in the broadband fitting. The energy of diffuse Fe<sub>XXV</sub> line is linked to that of the AGN component. Column (3): line width. These are fixed at the values reported in [Arévalo et al. \(2014\)](#) except for AGN Fe<sub>XXV</sub> line. The width of AGN 6.66 keV line is left free in the broadband fitting. Column (4): normalization of the lines. These were also left free in the broadband fitting. Lines whose best-fit normalizations are less than  $1.0 \times 10^{-10}$  were not included. Column (5): line ID.

<sup>a</sup>The parameter reaches a limit of its allowed range.

**Table 6.** Best Fit Parameters of Fe K $\alpha$  Line

$C_{2\text{nd}}$	$C_{3\text{rd}}$	$z_{2\text{nd}}$	$z_{3\text{rd}}$	$f_{\text{diff}}$	$\sigma_{\text{E}}^{\text{diff}}$ (eV)	$\log(r_{\text{in}}/r_{\text{g}})$	Norm.	C/dof
(1)	(2)	(3)	(4)	(5)	(6)	(7)	(8)	
$0.83^{+0.11}_{-0.10}$	$0.64^{+0.09}_{-0.08}$	$1.57^{+0.25}_{-0.25} \times 10^{-3}$	$1.53^{+0.25}_{-0.26} \times 10^{-3}$	$0.19^{+0.16}_{-0.09}$	$24.8^{+12.4}_{-7.7}$	$5.28^{+0.42}_{-0.23}$	$0.91^{+0.04}_{-0.04}$	98.8/100

NOTE— Columns (1) and (2): Cross-normalization factors for the second and third order spectra, respectively. Columns (3) and (4): Redshifts for the second and third order spectra, respectively. Column (5): Fraction of the extended emission. Column (6): Width of the spatial extent. Column (7): Torus inner radius in units of gravitational radius. Column (8): Normalization of xclumpyvd.L.fits.

### 6.2. Torus Inner Radius

We have performed a simultaneous spectral analysis of the Chandra/HETG first, second, and third order spectra of the Circinus galaxy, where we take into account the spatial extent of the Fe K $\alpha$  line emitting region. We obtain  $\log(r_{\text{in}}/r_{\text{g}}) = 5.28^{+0.42}_{-0.23}$ , which corresponds to a Keplerian velocity of  $690^{+200}_{-270}$  km s<sup>-1</sup> at the inner edge of the torus, and to  $r_{\text{in}} = 1.6^{+1.6}_{-0.9} \times 10^{-2}$  pc for an SMBH mass of  $(1.7 \pm 0.3) \times 10^6 M_{\odot}$  (Section 5.2). Our inner

radius is 2.5 times larger than that reported in [Shu et al. \(2011\)](#). This is most probably because they analyzed the first order spectrum by ignoring the spatial extent and fitted the Fe K $\alpha$  line with a single Gaussian model, both led them to overestimate the true line width. By contrast, the torus inner radius obtained here is consistent with the location of the Si K $\alpha$  line emitting region estimated by [Liu \(2016b\)](#) ( $0.03^{+0.06}_{-0.015}$  pc), which was later interpreted by [Liu et al. \(2019\)](#) to mainly originate from

the polar outflows. We note that our torus inner radius is smaller than the maser-disk radius ( $r = 0.11 \pm 0.02$  pc, Greenhill et al. 2003).

The innermost radius of the dusty region in a torus (dusty torus) can be estimated from the dust sublimation radius ( $R_{\text{sub}}$ ), the limit where dust grains can exist against radiative heating from the central engine. Nenkova et al. (2008a,b) derived the formula of the sublimation radius of a clumpy torus as:

$$R_{\text{sub}} = 0.4 \left( \frac{L_{\text{bol}}}{10^{45} \text{ erg s}^{-1}} \right)^{0.5} \left( \frac{1500 \text{ K}}{T_{\text{sub}}} \right)^{2.6} \text{ pc}, \quad (10)$$

where  $L$  is the bolometric luminosity of the AGN and  $T_{\text{sub}}$  is the sublimation temperature. Adopting  $T_{\text{sub}} = 1500$  K and the bolometric luminosity derived from the broadband spectral analysis (Section 4.2), we obtain that of the Circinus galaxy to be  $R_{\text{sub}} \sim 0.14$  pc. Kishimoto et al. (2007) found that the torus inner radius in an AGN derived from the near-infrared reverberation mapping was  $\sim 3$  times smaller than the sublimation radius calculated as above; the factor 3 difference can be explained by considering the anisotropy of emission from the accretion disk (Kawaguchi & Mori 2010). If we apply this relation, the inner radius of the dusty torus in the Circinus galaxy is estimated as  $\approx 0.05$  pc.

The torus inner radius we have derived from the Fe  $K\alpha$  line width is still significantly smaller than this value. Since the near-infrared reverberation observation only measures the location of dust, this result indicates that there is a significant amount of dust-free gas in the inner side of the dusty torus. Our result basically supports the arguments by Minezaki & Matsushita (2015) and Gandhi et al. (2015) that a significant fraction of the Fe  $K\alpha$  line originates from a region closer to the SMBH than the dusty torus. However, the torus inner radius we have derived is larger than these previous estimates, strongly suggesting that the region is well outside the broad line region. We note that our result is currently limited by the uncertainty of the spatial extent in analyzing the grating spectra. Future non-dispersive high resolution spectroscopy, like that by the X-Ray Imaging and Spectroscopy Mission (XRISM), will push forward

our understanding on the whole structure of an AGN including the torus and its inner region.

## 7. CONCLUSION

1. We update the XCLUMPY model developed by Tanimoto et al. (2019), an X-ray spectral model from a clumpy torus in an AGN, by incorporating line broadening effect due to the Keplerian rotation of the torus with variable metal abundance. This model enables us to constrain the inner radius of the torus from the fluorescence line profiles.
2. We apply the model to currently the best available broadband X-ray spectra (3–100 keV) of the Circinus galaxy. We confirm that the Circinus galaxy has a geometry thin and Compton-thick torus with super-solar ( $Z \approx 1.5$ ) metal abundance.
3. From the simultaneous analysis of the Chandra/HETG first, second, and third order spectra, we derive the torus inner radius emitting Fe  $K\alpha$  to be  $\log(r_{\text{in}}/r_{\text{g}}) = 5.28^{+0.42}_{-0.23}$  or  $1.6^{+1.6}_{-0.9} \times 10^{-2}$  pc, which is about 3 times smaller than that estimated from the dust sublimation radius. This suggests that the inner side of the torus is composed of dust-free gas.

This work has been financially supported by the Grant-in-Aid for Scientific 20H01946 (Y.U.) and for JSPS Research Fellowships 20J00119 (A.T.) and 19J22216 (S.Y.). This research has made use of data and software provided by the high energy astrophysics science archive research center (HEASARC) and the Chandra X-ray Center (CXC). We have also utilized the NASA/IPAC Extragalactic Database (NED).

*Facilities:* Suzaku, XMM-Newton, NuSTAR, Chandra

*Software:* HEASoft v6.27 (Nasa High Energy Astrophysics Science Archive Research Center (Heasarc) 2014), MONACO (Odaka et al. 2011, 2016), SAS v18.0.0 (Gabriel et al. 2004), CIAO v4.12, MARX (Davis et al. 2012), XSPEC (Arnaud 1996)

## APPENDIX

### A. EFFECT OF SPATIAL EXTENT IN HETG SPECTRA

Liu (2016a) reported that the width of Fe  $K\alpha$  line is often larger in the Chandra/HETG first order spectrum than in the second and third order spectra. It was

pointed out that the discrepancy can be explained by the spatial extent of the target<sup>9</sup>; the total broadening in physical coordinates  $x$  on the detector is given by

<sup>9</sup> [https://cxc.harvard.edu/newsletters/news\\_24/](https://cxc.harvard.edu/newsletters/news_24/)

$$\sigma_x^2 = \sigma_i^2 + \left(\frac{Rm\lambda}{pc}\right)^2 \sigma_v^2 + (F\sigma_\theta)^2 \quad (\text{A1})$$

where  $\sigma_i$  is the instrumental broadening,  $\sigma_v$  the intrinsic line width (Doppler broadening),  $\sigma_\theta$  the spatial extent,  $R$  the Rowland distance of the HETGS,  $m$  the grating order,  $\lambda$  the wavelength of the line,  $p$  the grating period, and  $F$  the focal length of the High Resolution Mirror Assembly (HRMA). (In Equation A1, we assume that all the broadening profile can be modelled by Gaussians.) In the standard processing, the response matrix is created by assuming a point source, and therefore the observed line width is given by

$$\sigma_v'^2 = \sigma_v^2 + \left(\frac{pc}{Rm\lambda}\right)^2 (F\sigma_\theta)^2 = \sigma_v^2 + \left(\frac{1750}{m}\sigma_\theta\right)^2, \quad (\text{A2})$$

where  $\sigma_v'^2$  and  $\sigma_v^2$  are given in units of  $\text{km s}^{-1}$  and  $\sigma_\theta$  in units of arcsec. This shows that the spatial broadening effect is inversely proportional to the grating order. In fact, if we ignored the effect of the spatial extent of Fe  $K\alpha$  line emitting region in the Circinus galaxy, we would obtain  $r_{\text{in}} = (5.6 \pm 1.4) \times 10^{-3}$  pc and  $r_{\text{in}} = (1.4 \pm 0.8) \times 10^{-2}$  pc from the first and second/third order spectra, respectively, consistent with the trend reported by Liu (2016a).

## B. DEPENDENCE OF TORUS INNER RADIUS ON RADIAL DENSITY PROFILE

We evaluate the dependence of the torus inner radius derived from the spectral analysis on the assumed radial profile index of clump number density ( $q$ ). Ichikawa et al. (2015) analyzed the infrared spectral energy distribution of the Circinus galaxy with the CLUMPY model and constrained  $q = 0.6 \pm 0.3$ . Following the result, we make three models with  $q = 0.3, 0.6,$  and  $0.9$ , and apply them to the 6.3–6.5 keV HETG spectra. The other model parameters are the same as those reported in Section 5.2.

Table 7 summarizes the result. We find that a model with a smaller value of  $q$  results in a smaller torus inner radius. However, we confirm that the difference is small and does not change our conclusion.

## C. DEPENDENCE ON METAL ABUNDANCE

Table 8 summarizes the results of the broadband spectral fitting in two different settings:  $Z = 1.0$  (fixed) and  $Z = 1.52$  (free, best-fit). We see that the supersolar abundance of the torus significantly improves the fit. Among the torus parameters, the hydrogen column density along the equatorial plane shows the largest difference. We interpret that, since the photoelectric absorption is well constrained by the spectra, which is dominated by metals, higher metallicity leads to a smaller

**Table 7.** Torus inner radius in various radial density profiles.

$q$	$\log(r_{\text{in}}/r_g)$
(1)	(2)
0.3	$5.19^{+0.31}_{-0.27}$
0.6	$5.27^{+0.36}_{-0.23}$
0.9	$5.30^{+0.38}_{-0.21}$

NOTE— Column (1): index of radial density profile. Column (2): torus inner radius in units of gravitational radius.

**Table 8.** Best-fit torus parameters in two different metal abundances.

$Z$	$N_{\text{H}}^{\text{Equ}}$	$\sigma$	$i$	$\chi^2/\text{dof}$
(1)	(2)	(3)	(4)	
1.0	$30.5^{+1.5}_{-1.9}$ <sup>a</sup>	$11.5^{+1.0}_{-0.9}$	$78.8^{+0.6}_{-0.7}$	2341/1992
$1.52^{+0.05}_{-0.06}$	$21.6^{+2.4}_{-1.7}$	$10.3^{+0.8}_{-0.3}$	$78.3^{+0.5}_{-0.9}$	2275/1992

NOTE— Column (1): metal abundance of the torus in units of solar abundance. Column (2): hydrogen column density along the equatorial plane in units of  $10^{24} \text{ cm}^{-2}$ . Column (3): torus angular width in units of degrees. Column (4): inclination angle in units of degrees.

<sup>a</sup>The parameter reaches a limit of its allowed range.

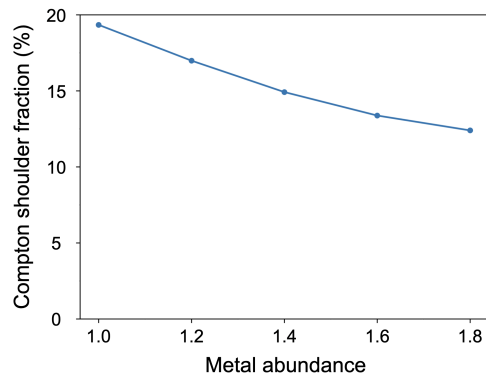


**Figure 7.** Dependence of the Compton-shoulder fraction on the metal abundance. We adopt the basic torus parameters:  $N_{\text{H}}^{\text{Equ}} = 2.0 \times 10^{25} \text{ cm}^{-2}$ ,  $\sigma = 10^\circ$ ,  $i = 78^\circ$ .

column density of hydrogen. The main driving factor that determines the metal abundance is the fraction of Compton shoulder in the Fe  $K\alpha$  line. Figure 7 shows the dependence of the Compton-shoulder fraction on the

metal abundance while the other torus parameters are kept the same. As seen, the Compton-shoulder fraction become smaller with increasing metal abundance.

#### D. FE $K\alpha$ LINE EMITTING REGION IN XCLUMPY

The ray-tracing simulations performed to make the XCLUMPY table model enable us to check the positions where the fluorescence lines are produced. The left and right panels of Figure 8 plot the last interaction points of the observed Fe  $K\alpha$  lines (except for the Compton shoulder) projected onto the equatorial plane (i.e.,

viewed from the polar axis direction) and onto a plane perpendicular to the line of sight (i.e., viewed from the observer), respectively, for 4 sets of the torus parameters ((1)–(4)). The left and right panels of Figure 9 display their azimuthal distribution and the radial profile of emissivity (photon numbers per unit area), respectively. For each parameter set, we fit the radial profile with a power-law, whose best fit result is overplotted. As noticed, when a Compton-thick torus is viewed nearly edge on, photons emitted from the far-side torus become dominant. Figure 10 shows the intrinsic Fe  $K\alpha$  line profiles.

#### REFERENCES

- Anders, E., & Grevesse, N. 1989, *GeoCoA*, 53, 197, doi: [10.1016/0016-7037\(89\)90286-X](https://doi.org/10.1016/0016-7037(89)90286-X)
- Arévalo, P., Bauer, F. E., Puccetti, S., et al. 2014, *ApJ*, 791, 81, doi: [10.1088/0004-637X/791/2/81](https://doi.org/10.1088/0004-637X/791/2/81)
- Arnaud, K. A. 1996, in *Astronomical Society of the Pacific Conference Series*, Vol. 101, *Astronomical Data Analysis Software and Systems V*, ed. G. H. Jacoby & J. Barnes, 17
- Baloković, M., Brightman, M., Harrison, F. A., et al. 2018, *ApJ*, 854, 42, doi: [10.3847/1538-4357/aaa7eb](https://doi.org/10.3847/1538-4357/aaa7eb)
- Bianchi, S., Matt, G., Fiore, F., et al. 2002, *A&A*, 396, 793, doi: [10.1051/0004-6361:20021414](https://doi.org/10.1051/0004-6361:20021414)
- Brightman, M., & Nandra, K. 2011, *MNRAS*, 413, 1206, doi: [10.1111/j.1365-2966.2011.18207.x](https://doi.org/10.1111/j.1365-2966.2011.18207.x)
- Brightman, M., Baloković, M., Stern, D., et al. 2015, *ApJ*, 805, 41, doi: [10.1088/0004-637X/805/1/41](https://doi.org/10.1088/0004-637X/805/1/41)
- Buchner, J., Brightman, M., Nandra, K., Nikutta, R., & Bauer, F. E. 2019, *A&A*, 629, A16, doi: [10.1051/0004-6361/201834771](https://doi.org/10.1051/0004-6361/201834771)
- Canizares, C. R., Davis, J. E., Dewey, D., et al. 2005, *PASP*, 117, 1144, doi: [10.1086/432898](https://doi.org/10.1086/432898)
- Cash, W. 1979, *ApJ*, 228, 939, doi: [10.1086/156922](https://doi.org/10.1086/156922)
- Davis, J. E., Bautz, M. W., Dewey, D., et al. 2012, in *Society of Photo-Optical Instrumentation Engineers (SPIE) Conference Series*, Vol. 8443, *Space Telescopes and Instrumentation 2012: Ultraviolet to Gamma Ray*, ed. T. Takahashi, S. S. Murray, & J.-W. A. den Herder, 84431A, doi: [10.1117/12.926937](https://doi.org/10.1117/12.926937)
- Fabbiano, G., Paggi, A., Karovska, M., et al. 2020, *ApJ*, 902, 49, doi: [10.3847/1538-4357/abb5ad](https://doi.org/10.3847/1538-4357/abb5ad)
- Freeman, K. C., Karlsson, B., Lynga, G., et al. 1977, *A&A*, 55, 445
- Fukazawa, Y., Mizuno, T., Watanabe, S., et al. 2009, *PASJ*, 61, S17, doi: [10.1093/pasj/61.sp1.S17](https://doi.org/10.1093/pasj/61.sp1.S17)
- Fukazawa, Y., Hiragi, K., Mizuno, M., et al. 2011, *ApJ*, 727, 19, doi: [10.1088/0004-637X/727/1/19](https://doi.org/10.1088/0004-637X/727/1/19)
- Furui, S., Fukazawa, Y., Odaka, H., et al. 2016, *ApJ*, 818, 164, doi: [10.3847/0004-637X/818/2/164](https://doi.org/10.3847/0004-637X/818/2/164)
- Gabriel, C., Denby, M., Fyfe, D. J., et al. 2004, in *Astronomical Society of the Pacific Conference Series*, Vol. 314, *Astronomical Data Analysis Software and Systems (ADASS) XIII*, ed. F. Ochsenbein, M. G. Allen, & D. Egret, 759
- Gandhi, P., Hönig, S. F., & Kishimoto, M. 2015, *ApJ*, 812, 113, doi: [10.1088/0004-637X/812/2/113](https://doi.org/10.1088/0004-637X/812/2/113)
- Garmire, G. P., Bautz, M. W., Ford, P. G., Nousek, J. A., & Ricker, George R., J. 2003, in *Society of Photo-Optical Instrumentation Engineers (SPIE) Conference Series*, Vol. 4851, *X-Ray and Gamma-Ray Telescopes and Instruments for Astronomy.*, ed. J. E. Truemper & H. D. Tananbaum, 28–44, doi: [10.1117/12.461599](https://doi.org/10.1117/12.461599)
- Greenhill, L. J., Booth, R. S., Ellingsen, S. P., et al. 2003, *ApJ*, 590, 162, doi: [10.1086/374862](https://doi.org/10.1086/374862)
- Harrison, F. A., Craig, W. W., Christensen, F. E., et al. 2013, *ApJ*, 770, 103, doi: [10.1088/0004-637X/770/2/103](https://doi.org/10.1088/0004-637X/770/2/103)
- Hikitani, M., Ohno, M., Fukazawa, Y., Kawaguchi, T., & Odaka, H. 2018, *ApJ*, 867, 80, doi: [10.3847/1538-4357/aae1fe](https://doi.org/10.3847/1538-4357/aae1fe)
- Ichikawa, K., Packham, C., Ramos Almeida, C., et al. 2015, *ApJ*, 803, 57, doi: [10.1088/0004-637X/803/2/57](https://doi.org/10.1088/0004-637X/803/2/57)
- Ikeda, S., Awaki, H., & Terashima, Y. 2009, *ApJ*, 692, 608, doi: [10.1088/0004-637X/692/1/608](https://doi.org/10.1088/0004-637X/692/1/608)
- Jansen, F., Lumb, D., Altieri, B., et al. 2001, *A&A*, 365, L1, doi: [10.1051/0004-6361:20000036](https://doi.org/10.1051/0004-6361:20000036)
- Kawaguchi, T., & Mori, M. 2010, *ApJL*, 724, L183, doi: [10.1088/2041-8205/724/2/L183](https://doi.org/10.1088/2041-8205/724/2/L183)
- Kawamuro, T., Izumi, T., & Imanishi, M. 2019, *PASJ*, 71, 68, doi: [10.1093/pasj/psz045](https://doi.org/10.1093/pasj/psz045)

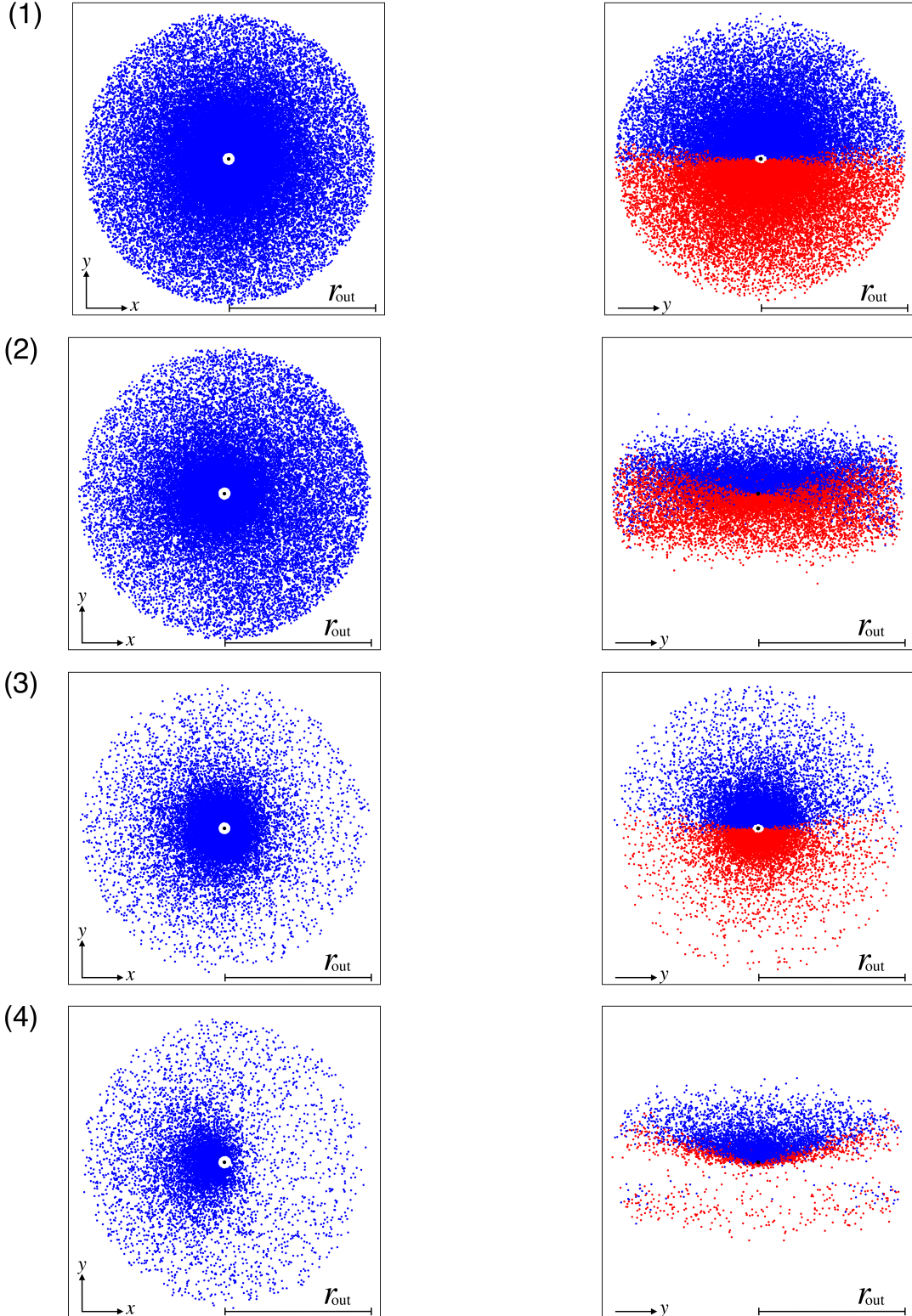


**Figure 8.** Maps of the Fe  $K\alpha$  line emitting region. The red and blue points represent the positions where observed Fe  $K\alpha$  photons (except for Compton shoulder) are originated. The central black points represent the SMBH. We set default torus parameters:  $Z = 1.5$ ,  $\sigma = 10^\circ$ . The other parameters are set to (1)  $N_{\text{H}}^{\text{Equ}} = 1.0 \times 10^{24} \text{ cm}^{-2}$ ,  $i = 30^\circ$ , (2)  $N_{\text{H}}^{\text{Equ}} = 1.0 \times 10^{24} \text{ cm}^{-2}$ ,  $i = 78^\circ$ , (3)  $N_{\text{H}}^{\text{Equ}} = 2.0 \times 10^{25} \text{ cm}^{-2}$ ,  $i = 30^\circ$ , and (4)  $N_{\text{H}}^{\text{Equ}} = 2.0 \times 10^{25} \text{ cm}^{-2}$ ,  $i = 78^\circ$ , from the top to the bottom. (Left): The positions projected onto the equatorial plane. An observer is viewing from the right direction. (Right): The positions viewed from the observer. The red and blue color represent the front side and the back side, respectively.

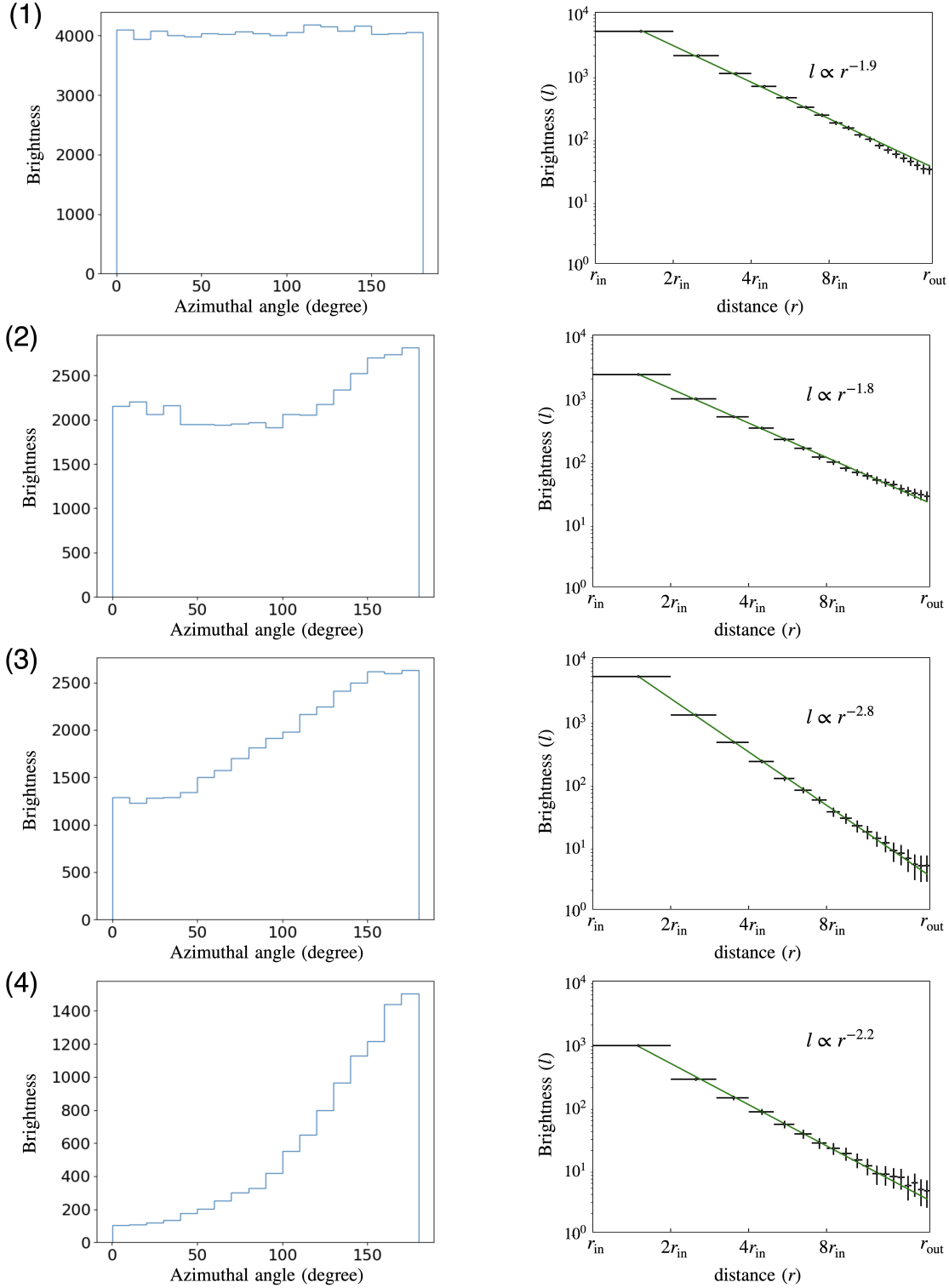


**Figure 9.** (Left): Azimuthal distribution of the Fe K $\alpha$  emitting positions projected onto the equatorial plane. The vertical axis is the number of photons (in an arbitrary unit), and the horizontal axis is the azimuthal angle with respect to the line of sight in degree. (Right): The radial profile. The vertical axis is the surface brightness ( $l$ ) in an arbitrary unit, and the horizontal axis is the distance from the SMBH  $r$ . The green lines represent the best-fit power-law models. The torus parameters are the same as in Figure 8.

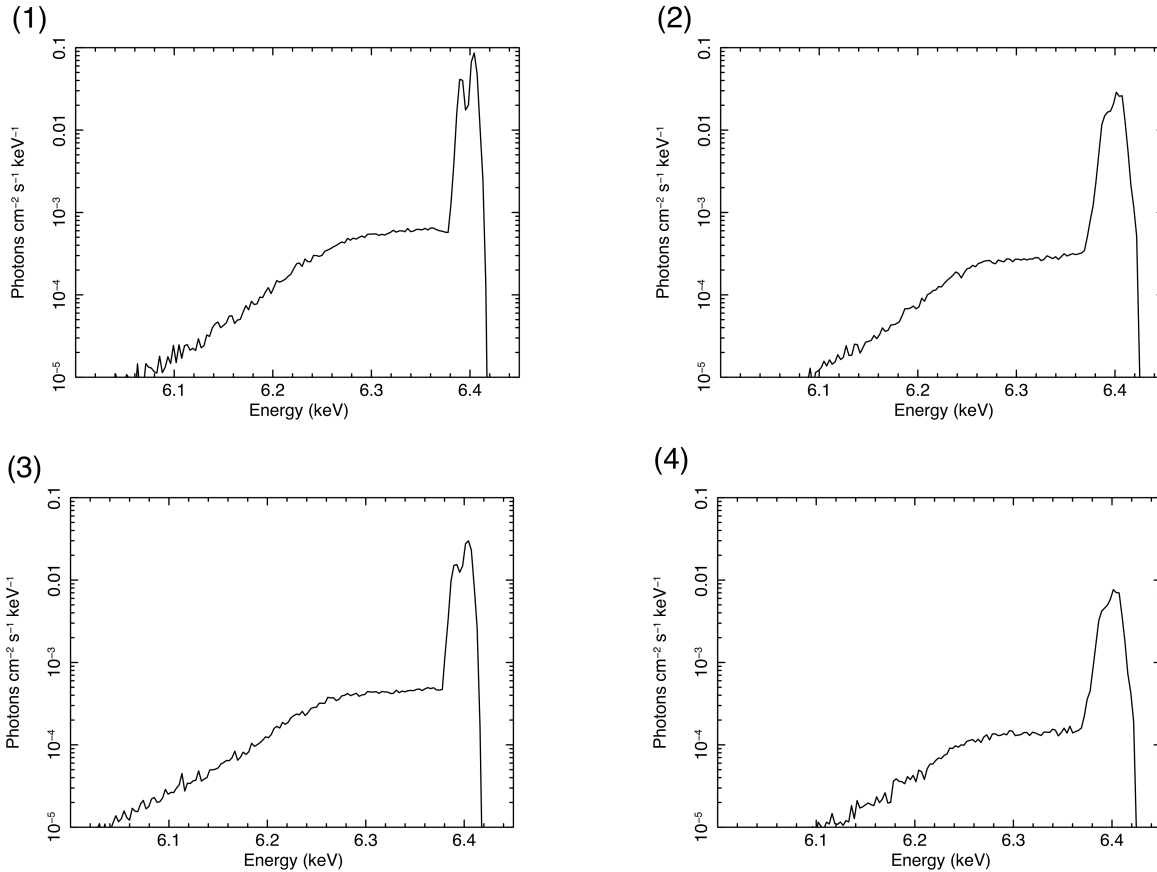


**Figure 10.** Fe  $K\alpha$  line profiles for the torus parameters in Figure 8. We assume  $\log(r_{\text{in}}/r_{\text{g}}) = 5.28$ .

Kawamuro, T., Ueda, Y., Tazaki, F., Ricci, C., & Terashima, Y. 2016, *ApJS*, 225, 14, doi: [10.3847/0067-0049/225/1/14](https://doi.org/10.3847/0067-0049/225/1/14)

Kishimoto, M., Hönig, S. F., Beckert, T., & Weigelt, G. 2007, *A&A*, 476, 713, doi: [10.1051/0004-6361:20077911](https://doi.org/10.1051/0004-6361:20077911)

Kokubun, M., Makishima, K., Takahashi, T., et al. 2007, *PASJ*, 59, 53, doi: [10.1093/pasj/59.sp1.S53](https://doi.org/10.1093/pasj/59.sp1.S53)

Kormendy, J., & Ho, L. C. 2013, *ARA&A*, 51, 511, doi: [10.1146/annurev-astro-082708-101811](https://doi.org/10.1146/annurev-astro-082708-101811)

Koshida, S., Yoshii, Y., Kobayashi, Y., et al. 2009, *ApJL*, 700, L109, doi: [10.1088/0004-637X/700/2/L109](https://doi.org/10.1088/0004-637X/700/2/L109)

Koyama, K., Tsunemi, H., Dotani, T., et al. 2007, *PASJ*, 59, 23, doi: [10.1093/pasj/59.sp1.S23](https://doi.org/10.1093/pasj/59.sp1.S23)

Liu, J. 2016a, *MNRAS*, 463, L108, doi: [10.1093/mnrasl/slw164](https://doi.org/10.1093/mnrasl/slw164)

—. 2016b, *MNRAS*, 459, L105, doi: [10.1093/mnrasl/slw048](https://doi.org/10.1093/mnrasl/slw048)

Liu, J., Hönig, S. F., Ricci, C., & Paltani, S. 2019, *MNRAS*, 490, 4344, doi: [10.1093/mnras/stz2908](https://doi.org/10.1093/mnras/stz2908)

Madsen, K. K., Beardmore, A. P., Forster, K., et al. 2017, *AJ*, 153, 2, doi: [10.3847/1538-3881/153/1/2](https://doi.org/10.3847/1538-3881/153/1/2)

Magdziarz, P., & Zdziarski, A. A. 1995, *MNRAS*, 273, 837, doi: [10.1093/mnras/273.3.837](https://doi.org/10.1093/mnras/273.3.837)

Marinucci, A., Miniutti, G., Bianchi, S., Matt, G., & Risaliti, G. 2013, *MNRAS*, 436, 2500, doi: [10.1093/mnras/stt1759](https://doi.org/10.1093/mnras/stt1759)

Markowitz, A. G., Krumpke, M., & Nikutta, R. 2014, *MNRAS*, 439, 1403, doi: [10.1093/mnras/stt2492](https://doi.org/10.1093/mnras/stt2492)

Massaro, F., Bianchi, S., Matt, G., D’Onofrio, E., & Nicastro, F. 2006, *A&A*, 455, 153, doi: [10.1051/0004-6361:20054772](https://doi.org/10.1051/0004-6361:20054772)

Minezaki, T., & Matsushita, K. 2015, *ApJ*, 802, 98, doi: [10.1088/0004-637X/802/2/98](https://doi.org/10.1088/0004-637X/802/2/98)

Mitsuda, K., Bautz, M., Inoue, H., et al. 2007, *PASJ*, 59, S1, doi: [10.1093/pasj/59.sp1.S1](https://doi.org/10.1093/pasj/59.sp1.S1)

Molendi, S., Bianchi, S., & Matt, G. 2003, *MNRAS*, 343, L1, doi: [10.1046/j.1365-8711.2003.06783.x](https://doi.org/10.1046/j.1365-8711.2003.06783.x)

Murphy, K. D., & Yaqoob, T. 2009, *MNRAS*, 397, 1549, doi: [10.1111/j.1365-2966.2009.15025.x](https://doi.org/10.1111/j.1365-2966.2009.15025.x)

Nasa High Energy Astrophysics Science Archive Research Center (Heasarc). 2014, *HEASoft: Unified Release of FTOOLS and XANADU*. <http://ascl.net/1408.004>

Nenkova, M., Sirocky, M. M., Ivezić, Ž., & Elitzur, M. 2008a, *ApJ*, 685, 147, doi: [10.1086/590482](https://doi.org/10.1086/590482)

- Nenkova, M., Sirocky, M. M., Nikutta, R., Ivezić, Ž., & Elitzur, M. 2008b, *ApJ*, 685, 160, doi: [10.1086/590483](https://doi.org/10.1086/590483)
- Odaka, H., Aharonian, F., Watanabe, S., et al. 2011, *ApJ*, 740, 103, doi: [10.1088/0004-637X/740/2/103](https://doi.org/10.1088/0004-637X/740/2/103)
- Odaka, H., Yoneda, H., Takahashi, T., & Fabian, A. 2016, *MNRAS*, 462, 2366, doi: [10.1093/mnras/stw1764](https://doi.org/10.1093/mnras/stw1764)
- Ogawa, S., Ueda, Y., Tanimoto, A., & Yamada, S. 2021, *ApJ*, 906, 84, doi: [10.3847/1538-4357/abcce](https://doi.org/10.3847/1538-4357/abcce)
- Qiu, Y., Soria, R., Wang, S., et al. 2019, *ApJ*, 877, 57, doi: [10.3847/1538-4357/ab16e7](https://doi.org/10.3847/1538-4357/ab16e7)
- Ramos Almeida, C., & Ricci, C. 2017, *Nature Astronomy*, 1, 679, doi: [10.1038/s41550-017-0232-z](https://doi.org/10.1038/s41550-017-0232-z)
- Reynolds, C., Ueda, Y., Awaki, H., et al. 2014, arXiv e-prints, arXiv:1412.1177. <https://arxiv.org/abs/1412.1177>
- Ricci, C., Trakhtenbrot, B., Koss, M. J., et al. 2017, *Nature*, 549, 488, doi: [10.1038/nature23906](https://doi.org/10.1038/nature23906)
- Sambruna, R. M., Netzer, H., Kaspi, S., et al. 2001, *ApJL*, 546, L13, doi: [10.1086/318068](https://doi.org/10.1086/318068)
- Shidatsu, M., Ueda, Y., & Fabrika, S. 2017, *ApJ*, 839, 46, doi: [10.3847/1538-4357/aa67e7](https://doi.org/10.3847/1538-4357/aa67e7)
- Shu, X. W., Yaqoob, T., & Wang, J. X. 2010, *ApJS*, 187, 581, doi: [10.1088/0067-0049/187/2/581](https://doi.org/10.1088/0067-0049/187/2/581)
- . 2011, *ApJ*, 738, 147, doi: [10.1088/0004-637X/738/2/147](https://doi.org/10.1088/0004-637X/738/2/147)
- Strüder, L., Briel, U., Dennerl, K., et al. 2001, *A&A*, 365, L18, doi: [10.1051/0004-6361:20000066](https://doi.org/10.1051/0004-6361:20000066)
- Takahashi, T., Abe, K., Endo, M., et al. 2007, *PASJ*, 59, 35, doi: [10.1093/pasj/59.sp1.S35](https://doi.org/10.1093/pasj/59.sp1.S35)
- Tanimoto, A., Ueda, Y., Kawamuro, T., et al. 2018, *ApJ*, 853, 146, doi: [10.3847/1538-4357/aaa47c](https://doi.org/10.3847/1538-4357/aaa47c)
- Tanimoto, A., Ueda, Y., Odaka, H., et al. 2019, *ApJ*, 877, 95, doi: [10.3847/1538-4357/ab1b20](https://doi.org/10.3847/1538-4357/ab1b20)
- . 2020, *ApJ*, 897, 2, doi: [10.3847/1538-4357/ab96bc](https://doi.org/10.3847/1538-4357/ab96bc)
- Turner, M. J. L., Abbey, A., Arnaud, M., et al. 2001, *A&A*, 365, L27, doi: [10.1051/0004-6361:20000087](https://doi.org/10.1051/0004-6361:20000087)
- Vasudevan, R. V., & Fabian, A. C. 2009, *MNRAS*, 392, 1124, doi: [10.1111/j.1365-2966.2008.14108.x](https://doi.org/10.1111/j.1365-2966.2008.14108.x)
- Walton, D. J., Harrison, F. A., Grefenstette, B. W., et al. 2014, *ApJ*, 793, 21, doi: [10.1088/0004-637X/793/1/21](https://doi.org/10.1088/0004-637X/793/1/21)
- Weisskopf, M. C., Brinkman, B., Canizares, C., et al. 2002, *PASP*, 114, 1, doi: [10.1086/338108](https://doi.org/10.1086/338108)
- Willingale, R., Starling, R. L. C., Beardmore, A. P., Tanvir, N. R., & O'Brien, P. T. 2013, *MNRAS*, 431, 394, doi: [10.1093/mnras/stt175](https://doi.org/10.1093/mnras/stt175)
- Yamada, S., Ueda, Y., Tanimoto, A., et al. 2020, *ApJ*, 897, 107, doi: [10.3847/1538-4357/ab94b1](https://doi.org/10.3847/1538-4357/ab94b1)
- Yang, Y., Wilson, A. S., Matt, G., Terashima, Y., & Greenhill, L. J. 2009, *ApJ*, 691, 131, doi: [10.1088/0004-637X/691/1/131](https://doi.org/10.1088/0004-637X/691/1/131)